

The Advection Boundary Law in absence of mean flow: passivity, nonreciprocity and enhanced noise transmission attenuation

Emanuele De Bono¹, **Manuel Collet**¹

¹ Ecole Centrale de Lyon, CNRS, ENTPE, LTDS,
UMR5513, 69130 Ecully, France
emanuele.de-bono@ec-lyon.fr

Morvan Ouisse²

² SUPMICROTECH, Université de Franche-Comté, CNRS,
institut FEMTO-ST, F-25000 Besançon, France.

March 18, 2024

Abstract

Sound attenuation along a waveguide is intensively studied for applications ranging from heating and air-conditioning ventilation systems, to aircraft turbofan engines. In particular, the new generation of Ultra-High-By-Pass-Ratio turbofan requires higher attenuation at low frequencies, in less space for liner treatment. This demands to go beyond the classical acoustic liner concepts and overcome their limitations. In this paper, we discuss an unconventional boundary operator, called Advection Boundary Law, which can be artificially synthesized by electroactive means, such as Electroacoustic Resonators. This boundary condition entails nonreciprocal propagation, meanwhile enhancing noise transmission attenuation with respect to purely locally-reacting boundaries, along one sense of propagation. Because of its artificial nature though, its acoustical passivity limits are yet to be defined. In this paper, we provide a thorough numerical study to assess the performances of the Advection Boundary Law, in absence of mean flow. An experimental test-bench validates the numerical outcomes in terms of passivity limits, non-reciprocal propagation and enhanced isolation with respect to local impedance operators. This work provides the guidelines to properly implement the Advection Boundary Law for optimal noise transmission attenuation. Moreover, the tools and criteria

provided here can also be employed for the design and characterization
of other innovative liners.

1 Introduction

The acoustic problem of interest here, is the noise transmission mitigation in an open duct, by treatment of the parietal walls with a so-called liner. Examples of industrial fields where this problem is particularly felt are the Heating and Ventilation Air-Conditioning Systems (HVAC) and the turbofan aircraft engines. The new generation of Ultra-High-Bypass-Ratio (UHBR) turbofans, in order to comply with the significant restrictions on fuel consumptions and pollutant emissions, present larger diameter, lower number of blades and rotational speed and a shorter nacelle. These characteristics conflict with the equally restrictive regulations on noise pollution, as the noise signature is shifted toward lower frequencies, which are much more challenging to be mitigated. The acoustic liner technology applied nowadays for noise transmission attenuation at the inlet and outlet portions of turbofan engines is the so-called Single or Multi-Degree-of-Freedom liner, whose working principle relates to the quarter-wavelength resonance, and demands larger thicknesses to target lower frequencies. They are made of a closed honeycomb structure and a perforated plate which is used to provide the dissipative effect, to add mass in order to decrease the resonance frequency, and also to maintain the aerodynamic flow as smooth as possible on the internal wall of the nacelle. As the honeycomb structure is impervious, propagation is prevented transversely to the wall, therefore it can be considered as *locally reacting* as long as the incident field wavelength is much larger than the size of the honeycomb cells [1].

A first interest for active control is the possibility to tune the resonators to different frequencies. Many adaptive Helmholtz resonator solutions have been proposed by varying either the acoustic stiffness (i.e. the cavity as in [2]), or the acoustic mass (i.e. the orifice area, as in [3]), or combining electroactive membranes with Helmholtz resonators [4], but these techniques tended to present complex structure, excessive weight and high energy consumption [1].

Active Noise Cancellation (ANC) has provided alternative solutions for achieving higher attenuation levels. From the seminal idea of Olson and May [5], first active *impedance control* strategies [6, 7] proposed an “active equivalent of the quarter wavelength resonance absorber” for normal and grazing incidence problems, respectively. The same technique was slightly

modified in [8], in the attempt to reproduce the Cremer’s liner optimal 64
impedance for the first duct modes pair [9, 10]. As such impedance could 65
not be achieved in a broadband sense, this approach remained limited to 66
monotonal applications. 67

These are examples of impedance control achieved through secondary source 68
approaches combined with passive liners, but the collocation of sensor and 69
actuator suggested also another avenue: the modification of the actuator 70
(loudspeaker or else) own mechano-acoustical impedance. The objective 71
shifts from creating a “quiet zone” at a certain location, to achieving an 72
optimal impedance on the loudspeaker diaphragm. This is the Electroa- 73
coustic Resonator (ER) idea, which have found various declinations, such 74
as electrical-shunting [11], direct-impedance control [12] and self-sensing 75
[13]. In order to overcome the low-flexibility drawback of electrical shunt- 76
ing techniques, minimize the number of sensors, meanwhile avoiding to 77
get involved into the electrical-inductance modelling of the loudspeaker, a 78
pressure-based current-driven architecture proved to achieve the best ab- 79
sorption performances in terms of both bandwidth and tunability [14]. It 80
employs one or more pressure sensors (microphones) nearby the speaker, 81
and a model-inversion digital algorithm to target the desired impedance by 82
controlling the electrical current in the speaker coil. Compared to classical 83
ANC strategies, the impedance control is conceived to assure the acoustical 84
passivity of the treated boundary, and hence the stability of the control 85
system independently of the external acoustic environment [15]. Despite the 86
physiological time delay of the digital control, which can affect the passivity 87
margins at high frequencies [16], such ER strategy has demonstrated its 88
efficiency for both room-modal equalization [17] and sound transmission 89
mitigation in waveguides [18, 19, 20, 21, 22]. The model-inversion algorithm 90
has also been extended to contemplate nonlinear target dynamics at low 91
excitation levels [23, 24, 25, 26]. 92

All the afore-mentioned boundary treatments for noise mitigation were con- 93
ceived in terms of target (locally-reacting) behaviors. In [27], for the first 94
time, a boundary operator involving the spatial derivative was targeted by 95
distributed electroacoustic devices. It was the first form of the Advection 96
Boundary Law (ABL), then implemented on ER arrays lining an acoustic 97
waveguide in [28, 29, 30], where it demonstrated non-reciprocal sound propa- 98
gation. Non-reciprocal propagation is a highly desirable feature for many 99
physical domains and applications [31]. In addition, the non-reciprocity 100
allows the ABL to potentially break through typical constraints on the 101
transmission attenuation of reciprocal media [32]. Nevertheless, because of 102
its spatial non-locality, the conceptual categories defining the passivity of 103

a surface impedance (see [33]) do not apply to the ABL. From that, comes the need to reformulate ad-hoc passivity conditions. Moreover, since the ABL lacks any analogue in nature, the physical interpretation of the ABL performances is not immediate. In addressing such points, overlooked in the previous references, is the main motivation and contribution of this manuscript.

Section 2 introduces the ABL from a theoretical point of view and provides a physical parallel which can help in the interpretation of the ABL performances. We arrive to a general definition of the ABL, composed of a convolution impedance operator ζ_{Loc} , and a convection term proportional to the advection speed U_b . In Section 3, the ABL is analysed in open-field to retrieve the oblique incidence absorption coefficient, as function of U_b and of the angle of the incident field. In Section 4, the duct-mode eigenproblem is solved by Finite Elements (FEs) for the first modes propagating in a 2D infinite waveguide lined on both sides by the ABL. A *modal* group velocity on the boundary is defined, which allows to introduce the *modal passivity*, as a relaxed version of the *absolute passivity* criteria. Moreover, the role played by the group velocity angle at the boundary gives the proper understanding of the physical mechanism behind the enhanced attenuation achieved with the ABL. The scattering performances are computed in Section 5 for a 2D duct in the plane wave regime without flow, and a very good correlation is observed with respect to the duct mode analysis. Then, in Section 6, we simulate a 3D waveguide lined by ERs synthesizing the ABL, confirming its enhanced isolation performances, along with its passivity issues. In Section 6, we also present the control law employed to enforce the ABL on the ERs. The effect of discrete pressure estimations by quasi-localized microphones, as well as the impact of time delay in the control algorithm, are briefly discussed. Finally, in Section 7, experimental results are provided to demonstrate the enhanced noise attenuation performances, the broadband nonreciprocal propagation, and the passivity limits of the ABL. The main novelties of this paper stay into the full characterization of the ABL and in the definition of a unique parameter to establish both passivity and noise isolation performances for grazing incidence problems. The nice physical interpretation provided by such parameter, can have an important impact in future designs of acoustic liners.

For the reader to easily keep track of the results along the way, at the end of some sections, we list the main outcomes provided there. The overall achievements and next steps are finally discussed in Section 8.

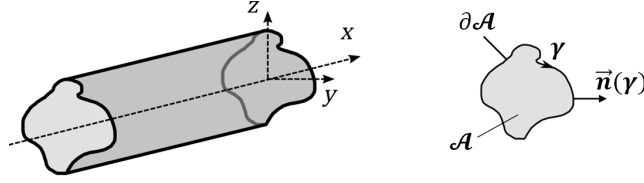


Figure 1. A cylindrical waveguide along coordinate x , with cross section \mathcal{A} of arbitrary shape. Left: overview of the waveguide. Right: detail of the cross-section and its contour $\partial\mathcal{A}$. $\vec{n}(\gamma)$ is the local exterior normal at each point of the contour, with tangential coordinate γ .

2 Theoretical conception

142

The greatest difficulty for the parietal treatment of a waveguide is, antono- 143
 matically, that it applies on the parietal walls $\partial\mathcal{A}$ (see Fig. 1), whereas the 144
 noise propagates along the longitudinal axis x which is clearly parallel to $\partial\mathcal{A}$. 145
 Such problem is usually referred to as *grazing incidence* problem. C. Bardos, 146
 G. Lebeau and J. Rauch [34] demonstrated that a sufficient condition for 147
 the boundary to fully control the wave propagation is that every ray of the 148
 acoustic field must interact with the boundary. But in case of the *grazing* 149
incidence problem, there will always be some rays not directly interacting 150
 with the boundary, therefore not *controllable*. This is also the reason why the 151
 effectiveness of any liner in noise transmission attenuation, degrades if the 152
 cross-section area of the waveguide increases, as less number of acoustic rays 153
 will directly interact with the boundary. Nevertheless, even if the grazing 154
 incidence problem is not fully controllable, it should still be possible to 155
 determine an optimal liner behaviour achieving the maximum attenuation of 156
 transmitted noise. 157

Morse [35], in 1939, recognized the normal surface impedance as the quantity 158
 characterizing the acoustic behaviour of a locally reacting boundary. It is 159
 defined as the ratio of Laplace transform of the local sound pressure and the 160
 normal velocity: $Z_s(s) = p(s)/v(s)$, where s is the Laplace variable, set to 161
 $j\omega$ (where $j = \sqrt{-1}$) in the stationary regime. However, a generic boundary 162
 might present non-locally reacting, non-linear or even time-variant acoustical 163
 response, and in that case the operator describing its acoustical behaviour 164
 cannot be reduced to an impedance transfer function. 165

The assumption of locally-reacting behaviour, and its consequent modelling 166
 by means of a surface impedance, is common practice in acoustics. Therefore, 167
 optimization theories have often considered locally-reacting behaviours of 168
 acoustic liners. This is the case for the Cremer's optimal impedance [9], 169

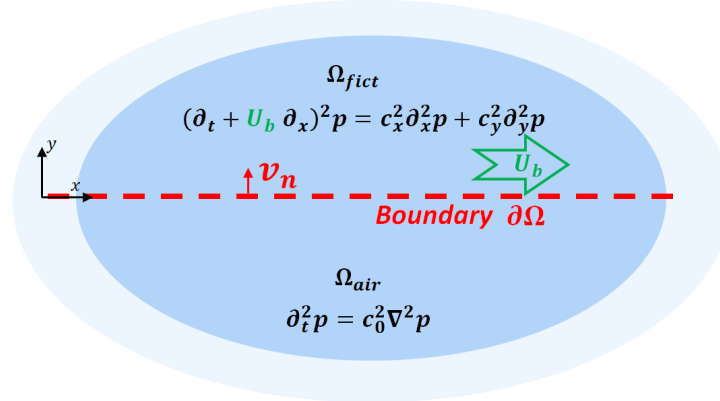


Figure 2. Interface $\partial\Omega$ between two semi-infinite domains: Ω_{air} and Ω_{fict} . Ω_{air} is filled with non-convected air, and extends indefinitely toward $\pm x$ and $-y$. Ω_{fict} extends indefinitely toward $\pm x$ and $+y$, and is an anisotropic acoustic medium characterized by Eq. (3).

after retrieved by Tester [10]. Such impedance, formulated in the frequency 170
domain, does not correspond to any real function in time domain (by inverse 171
Fourier transformation), as it does not satisfy the so-called reality condition 172
[33]. Attempts to achieve it in a broadband sense [36] resulted in very large 173
filters, limiting its practical implementation to single tones attenuation [37]. 174

To the authors knowledge, general spatial non-local operators have never 175
been targeted for sound transmission attenuation. Nevertheless, Morse 176
himself [35], in 1939, introduced the locally reacting surface as a degeneration 177
of a more general interface $\partial\Omega$ (see Fig. 2) between two propagative media. 178
The first one Ω_{air} is characterized by the wave equation in air: 179

$$c_0^2 \nabla^2 p = \partial_t^2 p \quad \text{in } \Omega_{air}, \quad (1)$$

with ∇ the Laplacian operator and c_0 the sound speed. The other 180
propagative domain, Ω_{fict} (fictitious) is represented by an anisotropic wave 181
equation, which in 2D reads: 182

$$c_x^2 \partial_x^2 p + c_y^2 \partial_y^2 p = \partial_t^2 p \quad \text{in } \Omega_{fict}, \quad (2)$$

where c_x and c_y are the phase speeds along the tangential x and normal 183
 y coordinates with respect to the boundary $\partial\Omega$. Observe that in [35], Eq. 184
(2) is written in terms of refractive indices rather than phase speeds. Let us 185
generalize such anisotropic wave equation to take into account a *convection* 186
speed U_b along x , in Ω_{fict} : 187

$$c_x^2 \partial_x^2 p + c_y^2 \partial_y^2 p = (\partial_t + U_b \partial_x)^2 p \quad \text{in } \Omega_{fict}. \quad (3)$$

Following Morse, a *locally reacting surface* could be interpreted as the interface between air and a domain Ω_{fict} , characterized by Eq. (3) with $c_x = U_b \ll c_y$, such that both convection and propagation along x can be neglected. This way, Eq. (3) *degenerates* into a 1D wave equation, where wave propagation in Ω_{fict} is allowed only along the normal direction y to the surface $\partial\Omega$, with a phase speed equal to c_y . The boundary $\partial\Omega$ would then be seen as a locally-reacting surface by Ω_{air} , with characteristic impedance $\rho_{fict} c_y$, with ρ_{fict} the density in Ω_{fict} . For Ω_{fict} extending to infinity along the $+y$ direction, then the characteristic impedance becomes the surface impedance of the locally-reacting surface $\partial\Omega$. By contemplating complex values of c_y and/or ρ_{fict} , complex impedances would be reproduced on the interface $\partial\Omega$. Usually, non-locally reacting surfaces are attained because c_x is different from zero in Eq. (3). It is the case of classical passive non-locally reacting liners (as porous layers), where the y -dimension of Ω_{fict} is bounded by a rigid back wall [38, 39].

In the following discussion, Ω_{fict} will be considered as extending indefinitely from the boundary $\partial\Omega$ toward both coordinate directions $(\pm x, +y)$, as showed in Fig. 2 for the 2D case. The definition of a boundary operator corresponding to a rear semi-infinite propagative domain is the so-called Dirichlet-to-Neumann (DtN) mapping [40], commonly employed in computational methods for simulating unbounded radiation. The DtN approach is retrieved in [27] where, by passing through the Fourier space, the pseudo-differential boundary operator (relating sound pressure and its normal derivative), which maps a semi-infinite domain Ω_{fict} on the interface with Ω_{air} , is computed in case of Ω_{fict} with same propagation characteristics as Ω_{air} ($c_y = c_x = c_0$, $U_b = 0$). Following the same steps as [27], we can enlarge the pseudo-differential operator presented in [27] to contemplate an anisotropic and convected propagation in Ω_{fict} as the one described by Eq. (3), and obtain:

$$c_y \partial_y p = - \left[\sqrt{(\partial_t + U_b \partial_x)^2 - c_x^2 \partial_x^2} \right] p \quad \text{on } \partial\Omega. \quad (4)$$

In case of $U_b = 0$ and $c_x = c_y$, we retrieve the pseudo-differential operator for perfect absorption given in [27], while in case of $c_x = U_b = 0$, we fall back into the local impedance operator. Observe that Eq. (4) gives the relationship between pressure and its normal derivative, at the interface with a propagative and convected medium. Such relationship is found by

imposing the continuity of pressure and normal velocity between the two media [35, 27]. In real life, the presence of convection and viscosity, would entail a vortex sheet [41, 42, 43] and the continuity of displacement, rather than velocity, at the interface. Nevertheless, as long as we are referring to a fictitious domain Ω_{fict} , this can be assumed inviscid and purely potential, and the continuity of velocity can be maintained as in [44].
 Supposing $c_x = 0$, Eq. (4) degenerates into:

$$c_y \partial_y p = -(\partial_t + U_b \partial_x) p \quad \text{on } \partial\Omega. \quad (5)$$

Eq. (5) is the ABL. **Therefore, we can finally interpret the ABL as the DtN map of a semi-infinite domain Ω_{fict} , characterized by potential wave propagation only along the direction y normal to the boundary (as for locally reacting surfaces), but where such propagation is convected along x with advection speed U_b .** Note that in [27], c_y was taken as equal to c_0 and Eq. (5) was not introduced as a degeneration of the general boundary operator (here provided in Eq. (4)) mapping a convected anisotropic domain on the boundary. Hence, the introduction of the ABL lacked of a proper physical interpretation. Using the Euler equation of acoustics projected along the y -axis (normal to $\partial\Omega$), in absence of mean-flow [45]:

$$\rho_0 \partial_t v_y = -\partial_y p, \quad (6)$$

with v_y the velocity along y (normal to the boundary), Eq. (5) writes:

$$\rho_0 c_y \partial_t v_y = \partial_t p + U_b \partial_x p \quad \text{on } \partial\Omega. \quad (7)$$

Observe that, for $U_b = 0$, Eq. (7) retrieves a locally reacting boundary of surface acoustic impedance $Z_{Loc} = \rho_0 c_y$. To introduce a general complex local impedance $Z_{Loc}(j\omega)$, we can define the corresponding differential operator in time domain $Z_{Loc}(\partial_t)$ (same notation as [46]), convoluting (*) the local normal acceleration $\partial_t v_y$. So, Eq. (7) rewrites:

$$Z_{Loc}(\partial_t) * \partial_t v_y = \partial_t p + U_b \partial_x p \quad \text{on } \partial\Omega. \quad (8)$$

In the following, the effects of such BC are investigated first analytically on a semi-infinite domain Ω_{air} , then numerically on a waveguide of infinite and finite lengths, finally experimentally in a duct lined by programmable ERs.

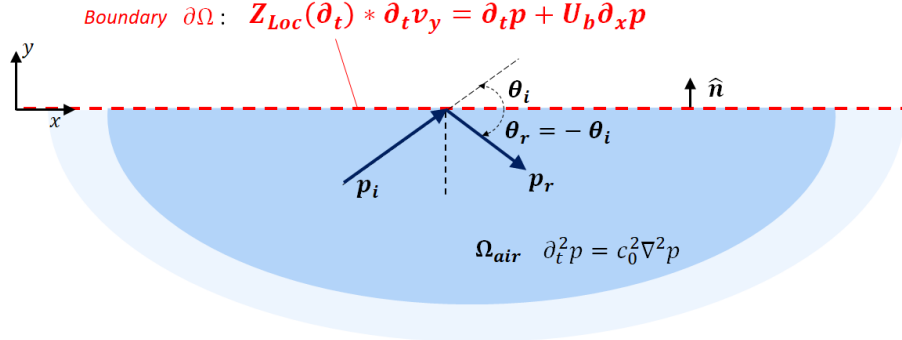


Figure 3. ABL interfacing a semi-infinite domain.

3 Advection Boundary Law in open field

249

As a first case study, we compute the absorption coefficient of the ABL interfacing a semi-infinite air domain (an open field), $\Omega_{air} = [-\infty, \infty] \times [-\infty, 0]$, as in Fig. 3. The treated boundary extends on all the x axis.

250

251

252

Assuming a time-harmonic sound field in the usual complex notation ($j\omega t$), the incident wave can be expressed as:

253

254

$$\bar{p}_i(t, \omega, x, y) = p_{i0}(\omega) e^{j\omega t - jk_0 \cos \theta_i x - jk_0 \sin \theta_i y}, \quad (9)$$

where \bar{p}_i is the complex representation of $p_i = \text{Re}\{\bar{p}_i\}$, $k_0 = \omega/c_0$ is the wavenumber of a plane wave, c_0 is the speed of sound, and θ_i is the incident angle of the plane wave on the treated boundary. The reflected wave field is supposed to respect the classical Snell-Descartes law of refraction, according to which the reflected plane wave propagates with a specular angle with respect to the incident one, i.e. $\theta_r = -\theta_i$. The presence of a transport at the boundary gives no reason to modify this assumption, in an analogous way to the case of air-flow in the acoustic domain [41], or to the case of interface with a convected propagative medium [43].

255

256

257

258

259

260

261

262

263

Hence, the complex reflected wave from an ABL can be written as:

264

$$\bar{p}_r(t, \omega, x, y) = R(j\omega) p_{i0} e^{j\omega t - jk_0 \cos \theta_i x + jk_0 \sin \theta_i y}, \quad (10)$$

with R the reflection coefficient at the oblique incidence θ_i . The acoustic velocity v_y normal to the boundary is obtained by the Euler equation of acoustics projected along y (Eq. (6)), with $p = p_i + p_r$. Replacing Eq.s (9) and (10) in p_i and p_r respectively, we find the normal complex velocity on the boundary $y = 0$:

265

266

267

268

269

$$\bar{v}_y(t, x) = \frac{\sin \theta_i}{\rho_0 c_0} p_{i0} \left(1 - R(j\omega)\right) e^{j\omega t - jk_0 \cos \theta_i x}. \quad (11)$$

Also, the ABL of Eq. (8) can be applied to the total pressure $p = p_i + p_r$ to give:

$$\bar{v}_y(t, x) = \frac{p_{i0}}{Z_{Loc}(j\omega)} \left(1 + M_b \cos \theta_i\right) \left(1 + R(j\omega)\right) e^{j\omega t - jk_0 \cos \theta_i x}, \quad (12)$$

where $M_b = U_b/c_0$. Equating Eq. (11) and (12), we find the reflection coefficient:

$$R(\omega) = \frac{1 - \left(1 - M_b \cos \theta_i\right) \eta_{Loc}(j\omega) / \sin \theta_i}{1 + \left(1 - M_b \cos \theta_i\right) \eta_{Loc}(j\omega) / \sin \theta_i}, \quad (13)$$

where $\eta_{Loc}(j\omega) = \rho_0 c_0 / Z_{Loc}(j\omega)$ is the normalized local mobility. Observe that for $M_b = 0$, the reflection coefficient of classical locally-reacting surfaces is retrieved. Eq. (13) suggests the possibility to define an *effective* normalized mobility $\eta_{eff}(j\omega, M_b, \theta_i) = \left(1 - M_b \cos \theta_i\right) \eta_{Loc}(j\omega)$, which is equivalent to the ABL operator for the far-field reflection from an infinite boundary $\partial\Omega$. Observe that η_{eff} depends also on M_b and θ_i . In particular, it is interesting to notice that for $M_b = -1$, if $\theta_i \rightarrow 0$ then $\eta_{eff} \rightarrow 2\eta_{Loc}$, whereas if $\theta_i \rightarrow \pi$ then $\eta_{eff} \rightarrow 0$. This result preliminarily demonstrates the non-reciprocal propagation achieved by the ABL in grazing incidence, which is treated in the next sections.

Based on η_{eff} , we can write the absorption coefficient:

$$\alpha(\omega) = \frac{4 \operatorname{Re}\{\eta_{eff}(j\omega, \theta_i, M_b) / \sin \theta_i\}}{\left|1 + \eta_{eff}(j\omega, \theta_i, M_b) / \sin \theta_i\right|^2}. \quad (14)$$

From Eq. (14), we can apply the classical passivity condition for locally-reacting boundaries [33] to $\eta_{eff}(j\omega, \theta_i, M_b)$:

$$\operatorname{Re}\left\{\eta_{eff}(j\omega, \theta_i, M_b)\right\} \geq 0 \quad \text{i.e.} \quad \operatorname{Re}\left\{\eta_{Loc}(j\omega)\right\} \left(1 - M_b \cos \theta_i\right) \geq 0. \quad (15)$$

Eq. (15) is valid as long as $\operatorname{Re}\{\eta_{Loc}(j\omega)\} \geq 0$ (the local impedance operator should be passive) and $M_b \leq 1/\cos \theta_i$. For the passivity to hold

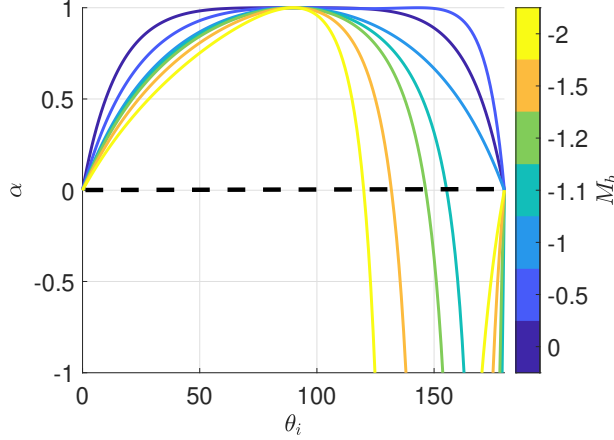


Figure 4. ABL absorption coefficient versus θ_i , in open field, for $\eta_{Loc} = 1$ and various $M_b \leq 0$.

independently of the angle of incidence, it must be $M_b \leq 1$. Such acoustical passivity condition signifies that acoustic energy *enters* the boundary, rather than being radiated from it. Let us write the acoustic intensity [45] normal to the boundary, I_y :

$$I_y(\omega) = \frac{1}{2} \text{Re}\{\bar{p}^*(\omega, x) \bar{v}_y(\omega, x)\} = \left(1 - |R(\omega)|^2\right) \frac{|p_{i0}(\omega)|^2}{2\rho_0 c_0} \sin \theta_i = \alpha(\omega) \frac{|p_{i0}(\omega)|^2}{2\rho_0 c_0} \sin \theta_i = \alpha(\omega) I_{i,y}(\omega), \quad (16)$$

where $I_{i,y}(\omega) = \frac{|p_{i0}(\omega)|^2}{2\rho_0 c_0} \sin \theta_i$ is the component along y of the incident acoustic intensity, and the superscript * indicates the complex conjugate. Therefore, for a given incident field, the normal component of the acoustic intensity gives the absorption at the boundary.

The ABL absorption coefficient versus the angle of incidence is plotted in Fig. 4 for $\eta_{Loc} = 1$ and different values of $M_b < 0$. Notice that the range of angles of incidence θ_i for which $\alpha < 0$, enlarges as $|M_b|$ is increased above 1. Moreover, such loss of acoustical passivity for $M_b < -1$, happens only for $\pi/2 < \theta_i < \pi$, meaning that the ABL is non-passive only for incident sound fields coming from the right side of Fig. 3, that is, for incident waves with $\text{sgn}(k_x) = \text{sgn}(M_b)$. The dependence upon the angle of incidence of ABL acoustical passivity is another unique feature of the ABL with respect to classical liners. This angle-of-incidence dependency of ABL acoustical passivity manifests in a duct-mode dependent stability, which is the subject of the next section.

Below, the main outcomes of Section 3:

- **In open field, the ABL passivity conditions are $\eta_{Loc} \geq 0$ and $|M_b| \leq 1$.**
- **In open field, the normal acoustic intensity at the boundary is related to the absorption coefficient of the boundary.**
- **In open field, ABL acoustical passivity depends upon the angle of the incident field.**
- **In open field, the passivity loss is larger for higher absolute values of $M_b < -1$.**

4 Duct modes analysis in 2D waveguide

After having defined the passivity condition of the ABL on a semi-infinite domain, let us investigate the passivity and attenuation performances into an acoustic waveguide starting from the duct mode analysis. Duct modes are fundamental to understand the propagation characteristics in a waveguide. The general formulation of the duct-mode eigen-problem is provided in Appendix A, along with the special treatment reserved to the ABL for the FE numerical resolution of our eigen-problem. The FE mesh has been built sufficiently fine to have large number of elements in the cross section and accurately resolve for each duct-mode shape of interest. We consider a 2D duct of section width $h = 0.05$ m, with both upper and lower walls lined by the ABL. According to the assumption of duct mode eigen-solution $\bar{p}_m(t, \omega, x, y) = A_m \psi_m(y, \omega) e^{j\omega t - jk_{x,m}(\omega)x}$, the duct mode analysis consists in computing the duct-mode eigenvalues ($k_{x,m}$) and eigenvectors (ψ_m), while A_m can be normalized at will. The duct-mode representation of the acoustic field, gives the occasion to define *modal acoustic intensities* and *modal group velocities*. In particular, the *local* modal acoustic intensity vector is given by:

$$\vec{I}_m(x, y, \omega) = \frac{1}{2} \text{Re}\{\bar{p}_m^*(t, \omega, x, y) \vec{v}_m(t, \omega, x, y)\}, \quad (17)$$

where the superscript $*$ indicates the complex conjugate, and \vec{v}_m is the modal acoustic velocity, related to the modal acoustic pressure \bar{p}_m by the Euler equation of acoustics $-\rho_0 j \omega \vec{v}_m = \vec{\nabla} \bar{p}_m$, where $\vec{\nabla}$ is the gradient operator. We can then compute the x and y components of \vec{I}_m :

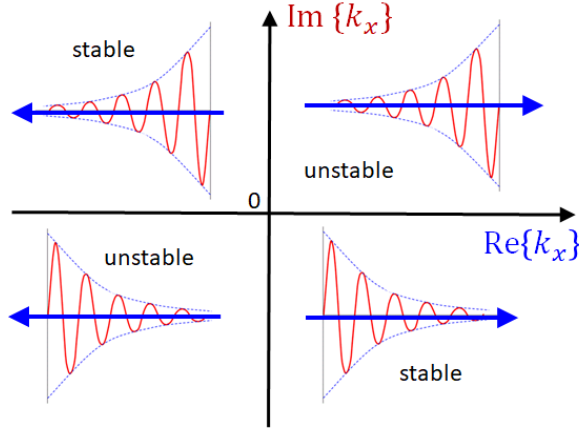


Figure 5. Stability regions of duct-modes in the $(\text{Re}\{k_x\}, \text{Im}\{k_x\})$ -plane.

$$I_{x,m}(x, y, \omega) = e^{2\text{Im}\{k_{x,m}x\}} \frac{1}{2\rho_0 c_0} \frac{\text{Re}\{k_{x,m}\}}{k_0} |\psi_m(y, \omega)|^2 \quad (18a)$$

339

$$I_{y,m}(x, y, \omega) = e^{2\text{Im}\{k_{x,m}x\}} \frac{1}{2\rho_0 c_0} \text{Re}\left\{ \psi_m^*(y, \omega) \partial_y \psi_m(y, \omega) \right\} \quad (18b)$$

We can now define the *average* acoustic intensity vector on the duct cross section:

340
341

$$\vec{I}_{m,Ave}(x, \omega) = \frac{1}{h} \int_0^h \vec{I}_m(x, y, \omega) dy. \quad (19)$$

It is easy to verify that, for symmetric duct modes (for which $\psi_m(h, \omega) = \psi_m(0, \omega)$), we get $\int_0^h I_{y,m}(x, y, \omega) dy = 0$. So:

342

343

$$\vec{I}_{m,Ave}(\omega) = \frac{1}{h} \left(\int_0^h I_{x,m}(y, \omega) dy \right) \vec{x} = e^{2\text{Im}\{k_{x,m}x\}} \frac{1}{2h\rho_0 c_0} \frac{\text{Re}\{k_{x,m}\}}{k_0} \left(\int_0^h |\psi_m(y, \omega)|^2 dy \right) \vec{x}, \quad (20)$$

where \vec{x} is the unit vector along x .

344

We can now define the local modal group velocity as:

345

$$\vec{c}_m(y, \omega) = \frac{\vec{I}_m(x, y, \omega)}{E_{m,Ave}(x, \omega)}, \quad (21)$$

where $E_{m,Ave}(x, \omega)$ is the average modal kinetic energy, defined as:

346

$$\begin{aligned}
E_{m,Ave}(x, \omega) &= \frac{\rho_0}{2h} \int_0^h \vec{v}_m^* \cdot \vec{v}_m dy \\
&= \frac{e^{2\text{Im}\{k_{x,m}x\}}}{2h\rho_0c_0^2} \left(\frac{|k_{x,m}|^2}{k_0^2} \int_0^h |\psi_m(y, \omega)|^2 dy + \frac{1}{k_0^2} \int_0^h |\partial_y \psi_m(y, \omega)|^2 dy \right).
\end{aligned} \tag{22}$$

We can then compute the average modal group velocity:

347

$$\begin{aligned}
\vec{c}_{m,Ave}(\omega) &= \frac{1}{h} \int_0^h \vec{c}_m(x, y, \omega) dy = \frac{1}{h} \frac{\int_0^h \vec{I}_m(x, y, \omega) dy}{E_{m,Ave}(x, \omega)} \\
&= c_0 \frac{\text{Re}\{k_{x,m}(\omega)\}}{k_0} \left(\frac{\int_0^h |\psi_m(y, \omega)|^2 dy}{\frac{|k_{x,m}|^2}{k_0^2} \int_0^h |\psi_m(y, \omega)|^2 dy + \frac{1}{k_0^2} \int_0^h \partial_y |\psi(y, \omega)|^2} \right) \vec{x},
\end{aligned} \tag{23}$$

Observe that neither the local or the average modal group velocities depend upon x . From the average modal group velocity expression, we can deduce that each duct mode propagates along x with a sign given by $\text{Re}\{k_{x,m}\}$, i.e. $\text{Re}\{k_{x,m}\} > 0$ means a $+x$ direction of propagation, and vice-versa. The $\text{Im}\{k_{x,m}\}$ instead, gives the attenuation (or amplification) rate of the modal acoustic intensity along the duct mode x -propagation, as it can be seen from the Eq. (20). The regions of duct-mode stability are illustrated in Fig. 5, for clarity. However, we are interested in defining a unique dimensionless quantity able to characterize both the attenuation and stability of a duct mode. Inspired by the work of Rice [47], we propose to consider the propagation angle of the local modal group velocity at the boundary, given by:

$$\theta_{b,m}(\omega) = \text{atan} \left(\frac{c_{n,m}(\omega, y_b)}{c_{x,m}(\omega, y_b)} \right), \tag{24}$$

where $c_{n,m}$ is the local modal group velocity component along the normal \vec{n} to the boundary, and y_b is the value of the y coordinate at the boundary. Clearly, a dissipative liner entails acoustic intensity that enters the boundary, i.e. a positive $c_{n,m}(\omega, y_b)$ and a $0 < \theta_{b,m} < \pi$. Therefore, we propose to define the following *absolute* acoustical passivity criteria of a generic BC for in-duct grazing-incidence problems:

$$\sin \theta_{b,m}(\omega) \geq 0, \quad \forall \omega > 0 \quad \text{and} \quad \forall m \in \mathbb{Z}^+. \tag{25}$$

Such *absolute* passivity criteria could be relaxed to introduce a more general *modal* acoustic passivity criteria:

$$\sin \theta_{b,m}(\omega) \geq 0 \quad \forall \omega > 0 \quad \text{and certain } m \in \mathbb{Z}^+, \quad (26)$$

Such quantity $\sin \theta_{b,m}$ very well correlates also with the attenuation levels achieved by the ABL, as it will be showed in the following. Observe that this quantity differs from the modal propagation angle considered by Rice [47] to correlate with the acoustic liner performances. In [47], the modal propagation angle at the boundary was computed from the wavenumber, and not from \vec{c}_m . Indeed, the group velocity was considered only in case of air-flow in the duct. Moreover, he proposed a geometric approach employing the open-field reflection coefficient computed for an incident angle equal to such modal propagation angle, to estimate the attenuation rate along the duct, achieving good approximation only for nearly hard walls (locally-reacting liners with $\eta_{Loc} \approx 0$). Moreover, the separation between incident and reflected fields cannot be operated in a duct-mode analysis, therefore such open-field reflection coefficient actually provides very poor estimations of the attenuation rates for general BCs of interest.

The solutions, both in terms of wavenumbers $k_{x,m}$ and mode-shapes $\psi_m(y)$ reported here, are computed for a 2D waveguide with cross section width $h = 0.05$ m (to conform with the experimental test-rig of Section 7), lined on both sides by our ABL. The results will be accompanied by the plots of $\sin \theta_{b,m}$ to demonstrate the perfect correlation of duct-mode stability with the modal passivity criteria of Eq. (26), and the good correlation with the attenuation rate given by $\text{Im}\{k_{x,m}\}$.

4.1 Real local impedance ζ_{Loc}

In this Section, the local impedance, and hence the local normalized mobility η_{Loc} , is considered as purely real.

In Figs 6 and 7 the first eight solutions in terms of wavenumbers and corresponding duct modes respectively, are plotted. The frequency span is limited between 150 and 3000 Hz to focus on the same frequency range as the experimental results. It is evident that the mode-shapes propagating towards $+x$ present a shorter wavelength along y with respect to those propagating toward $-x$. Moreover, one can notice that mode 1^+ is attenuated ($\text{Im}\{k_{x,1^+}\} < 0$), while mode 1^- is a plane wave ($\psi_1^- = 1, k_{x,1^-} = -k_0$). This demonstrates *the breaking of the reciprocity principle* [48] in the plane wave

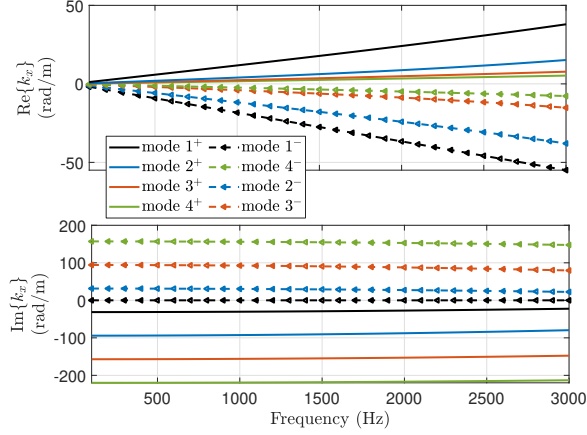


Figure 6. Dispersion plots for the wavenumbers relative to the first four duct modes propagating in both senses, in case of boundary advection law with $\eta_{Loc} = 1$ and $M_b = -1$.

regime, as it will be clearer in the following.

In this paper we study just the first forward and backward propagating mode (1^+ and 1^-), as we are interested in the isolation performances in the plane wave regime of a rigid duct. Indeed, the first modes are also the least attenuated ones, therefore mostly ruling the noise transmission when the liner is applied in a segment of a rigid duct [49, 9]. Fig. 8 shows the frequency plots of $\sin \theta_{b,m}$, $\text{Re}\{k_{x,m}\}$ and $\text{Im}\{k_{x,m}\}$, for modes $m = 1^+$ and $m = 1^-$. Looking at Fig. 8b, we observe that for $M_b = -1$, mode 1^- becomes a plane wave, while for $M_b < -1$ we have non-stable duct mode propagation, confirmed by a $\sin \theta_{b,1^-} < 0$. Notice that the attenuation rate ($\text{Im}\{k_{x,1^-}\}$) follows the same trend as $\sin \theta_{b,1^-} < 0$ with M_b , and also with frequency. Looking at Fig. 8a, notice the monotonic increase of both $\sin \theta_{b,1^+}$ and $\text{Im}\{k_{x,1^+}\}$ with $|M_b|$, confirming the good correlation between these two quantities, and the higher attenuation performances achievable thanks to the ABL with $M_b < 0$ with respect to local impedance operators ($M_b = 0$). Nevertheless, at high frequencies, $\text{Im}\{k_{x,1^+}\}$ for $M_b = -1.5$ seems to almost coalesce with $M_b = -1$ and $M_b = -0.5$, which is not the same for $\sin \theta_{b,1^+}$. We can then state that the correlation between $\sin \theta_{b,1^+}$ and the attenuation rate is very high at lower frequencies.

Fig. 9a shows the variation of the mode 1^+ shapes for various ABL Mach numbers $M_b < 0$, at 500 Hz. Looking at the mode-shapes $\psi_{1^+}(y)$, it is evident

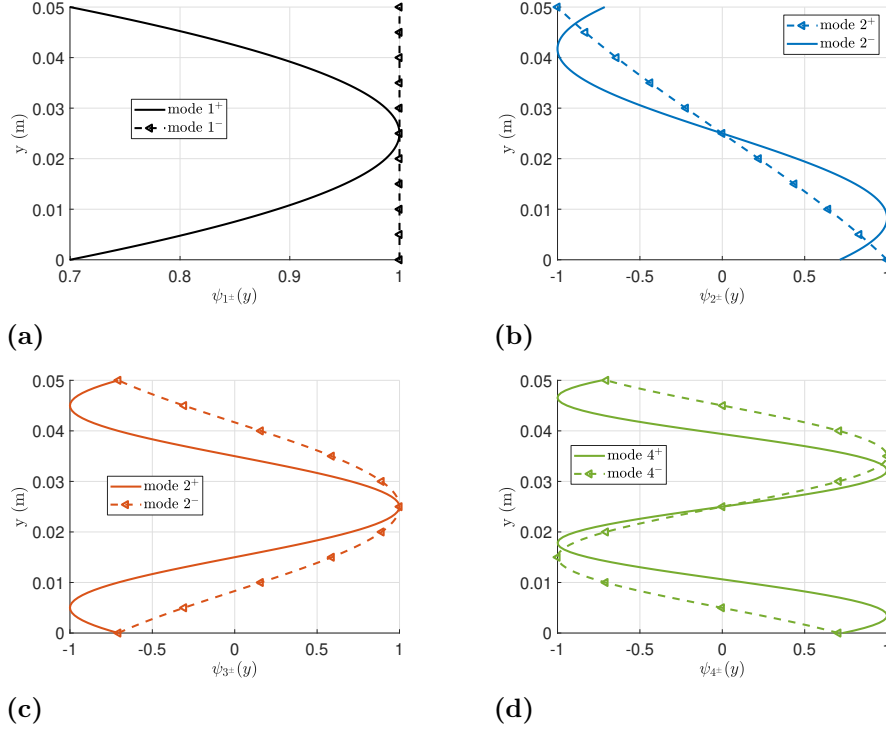


Figure 7. First four duct mode-shapes $\psi_m(y)$, propagating toward positive and negative x direction, normalized with respect to the maximum value, for ABL treated boundaries with $\eta_{Loc} = 1$ and $M_b = -1$, at 500 Hz.

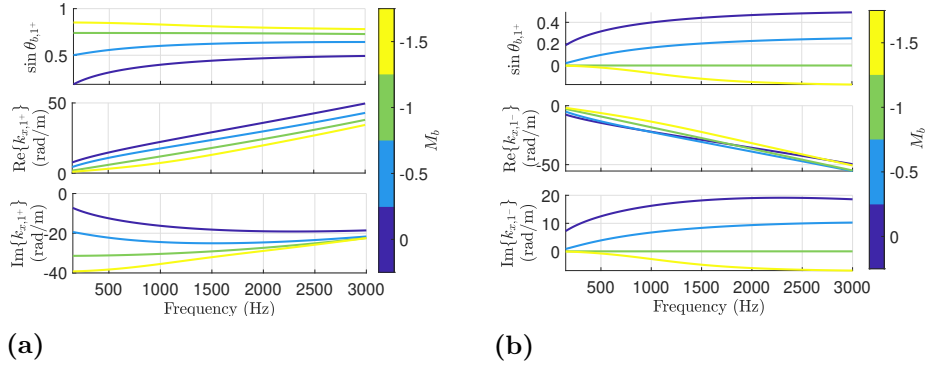


Figure 8. Spectra of $\sin \theta_{b,m}$, $\text{Re}\{k_{x,m}\}$ and $\text{Im}\{k_{x,m}\}$, with $\eta_{Loc} = 1$ and varying $M_b < 0$, for mode $m = 1^+$ (a) and $m = 1^-$ (b).

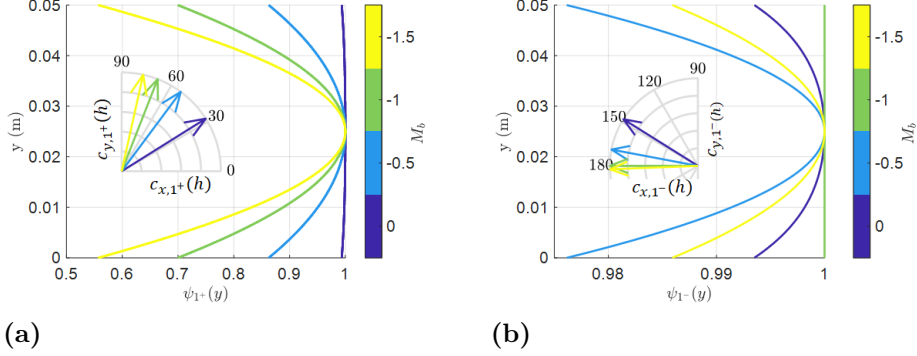


Figure 9. Shapes of modes 1^+ (a) and 1^- (b) at 500 Hz, and corresponding polar plots of the group velocities normalized to 1, for $\eta_{Loc} = 1$ and different $M_b < 0$.

how the wavelength along y is significantly reduced for higher absolute values of $M_b < 0$. This means a higher normal derivative at the boundary, hence an increase in the modal group velocity along y . The normalized vectors \vec{c}_{1^+} at the boundary $y_b = h$ are also reported in Fig. 9a to illustrate their rotation with M_b varying. For higher absolute values of $M_b < 0$, the modal group velocity at the boundary rotates towards the normal to the boundary itself. Fig. 9b shows the mode 1^- shapes for various ABL Mach numbers $M_b < 0$, at 500 Hz. Observe that for $M_b = -1$, $\psi_{1^-} = 1$ is a plane wave, with group velocity at the boundary directed toward $-x$. Notice also that for $M_b = -1.5$, $c_{1^-}(h)$ has a slightly negative component along y . Indeed, for $M_b < -1$, it is $\sin \theta_{b,1^-} < 0$ and the propagation of mode 1^- is unstable. Now, we want to check the effect of $\eta_{Loc} = 1/\zeta_{Loc}$ on the attenuation performances and passivity limits. In Fig. 10, the spectra of $\sin \theta_{b,m}$, $\text{Re}\{k_{x,m}\}$ and $\text{Im}\{k_{x,m}\}$, with varying η_{Loc} and $M_b = -1$, are plotted for mode $m = 1^+$. Observe that both $\sin \theta_{b,1^+}$ and $|\text{Im}\{k_{x,1^+}\}|$ increases with η_{Loc} , though the tendency with frequency is different especially at high frequencies as already noticed before. Moreover, η_{Loc} does not affect the stability of mode 1^+ for $M_b = -1$. Fig. 10 shows the same plots but relative to mode 1^- . Observe how η_{Loc} has no impact on such mode in case of $M_b = -1$. Indeed, for $M_b = -1$, mode 1^- is a plane wave independently of the value assumed by η_{Loc} .

In Fig. 12, the same quantities are plotted but for a fixed frequency (500 Hz), against η_{Loc} and for varying $M_b < 0$, for mode 1^+ . Apparently, increasing η_{Loc} improves the attenuation level of mode 1^+ , and its stability is preserved. Fig. 12 reports the same plots but for mode 1^- . Notice the

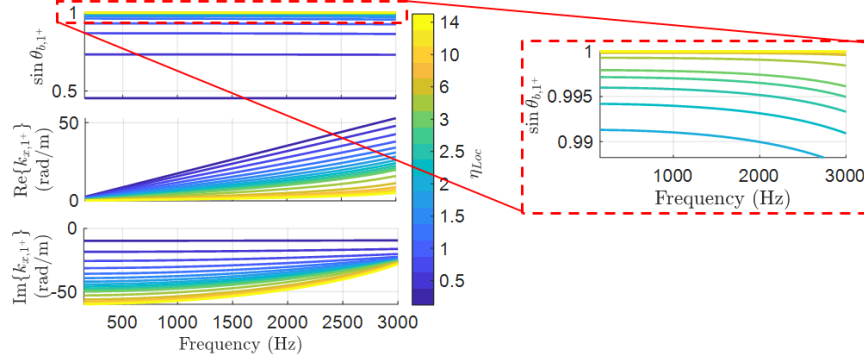


Figure 10. Spectra of $\sin \theta_{b,m}$, $\text{Re}\{k_{x,m}\}$ and $\text{Im}\{k_{x,m}\}$, with varying η_{Loc} and $M_b = -1$, for mode $m = 1^+$. On the right the zoom of $\sin \theta_{b,1^+}$ close to 1.

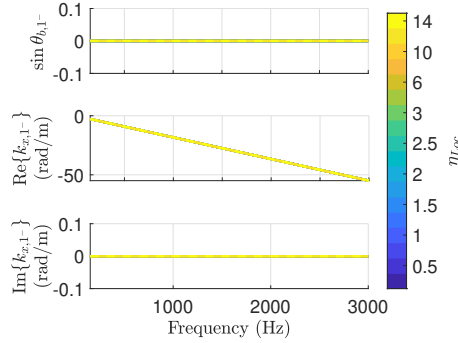


Figure 11. Spectra of $\sin \theta_{b,m}$, $\text{Re}\{k_{x,m}\}$ and $\text{Im}\{k_{x,m}\}$, with varying η_{Loc} and $M_b = -1$, for mode $m = 1^-$

plane wave solution ($k_{x,1^-} = -k_0$) for $M_b = -1$ which is independent from η_{Loc} . Also notice that the stability of mode 1^- is lost when $M_b < -1$, independently of η_{Loc} , as long as η_{Loc} is purely real and positive. This result confirms the passivity limits found in open field (see Eq. (15)). Hence, we can finally affirm that the ABL passivity limits in open-field (see Section 3) coincides with the absolute passivity limits of the ABL in the guided grazing incidence problem, in case of purely real η_{Loc} .

In Fig. 14a, we report the mode 1^+ shapes for $M_b = -1$ and varying η_{Loc} , along with the modal group velocity at the boundary. These plots help to visualize the effect of increasing η_{Loc} , which is very similar to the increase of the absolute value of $M_b < 0$, as long as mode 1^+ is concerned. Fig. 14a confirms that mode 1^- stays a plane wave independently of η_{Loc} , as long as

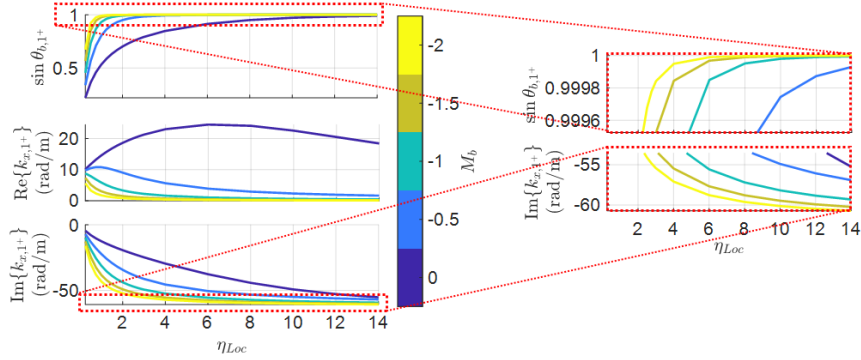


Figure 12. Plots of $\sin \theta_{b,m}$, $\text{Re}\{k_{x,m}\}$ and $\text{Im}\{k_{x,m}\}$, versus η_{Loc} , with varying $M_b < 0$, for mode $m = 1^+$. On the right the zoom of $\sin \theta_{b,m}$ close to the maximum value, and $\text{Im}\{k_{x,m}\}$ close to the minimum value.

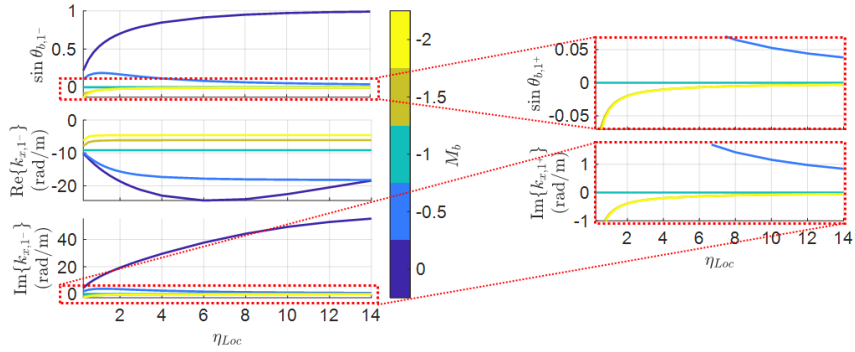


Figure 13. Plots of $\sin \theta_{b,m}$, $\text{Re}\{k_{x,m}\}$ and $\text{Im}\{k_{x,m}\}$, versus η_{Loc} , with varying $M_b < 0$, for mode $m = 1^-$. On the right the zoom of $\sin \theta_{b,m}$ and $\text{Im}\{k_{x,m}\}$ close 0.

$$M_b = -1.$$

From the duct mode analysis presented in this section, in case of purely real η_{Loc} , we can affirm that the ABL absolute passivity limits coincide with the passivity limits in open field. The physical quantity $\sin \theta_{b,m}$, other than allowing to define a modal passivity criteria, very well correlates with the attenuation rates for mode 1^+ , and could hence be employed for optimization purposes. Moreover, it can help in the interpretation of the physical mechanism behind the enhancement of the attenuation rate achieved by the ABL with respect to purely local impedances. The physical explanation of the influence of M_b upon the modal propagation angle at the boundary

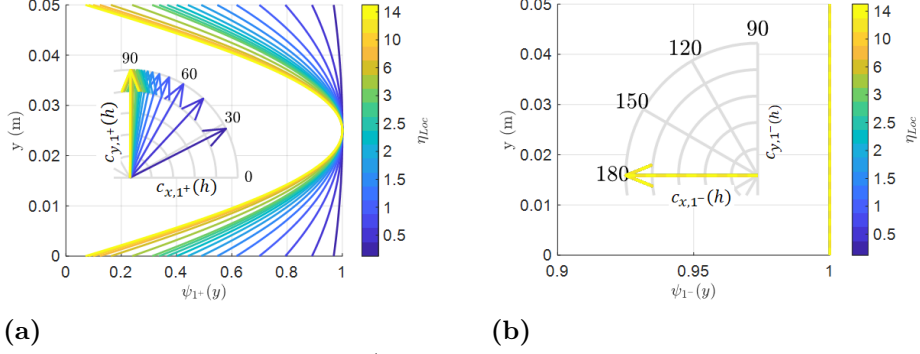


Figure 14. Shapes of modes 1^+ (a) and 1^- (b) at 500 Hz, and corresponding polar plots of the group velocities normalized to 1, for $M_b = -1$ and different η_{Loc} .

results to be quite intuitive, if compared to the instance of natural convection induced by air-flow blowing into a duct. In that case, waves are naturally convected downstream, with the modal propagation angle increasing for upstream propagating modes [47]. This phenomenon explains why, when the duct boundaries are treated by (reciprocal) acoustic liners, and in presence of air-flow, the upstream propagation is more attenuated with respect to the downstream one. In our case, there is no air-flow blowing in the duct. Nevertheless, we can induce an increase of the propagation angle of mode 1^+ at the boundary, for a fixed η_{Loc} , by introducing an artificial boundary convection against the propagation of mode 1^+ . This is what an ABL does with $M_b < 0$.

4.2 Complex local impedance ζ_{Loc}

In this Section, the local impedance component of the ABL is taken as a SDOF resonator, which is the case for most of the actual tunable liners, as the ERs. The mass and stiffness terms of ζ_{Loc} are taken proportional to the acoustic mass and stiffness of the open-circuit ER prototype employed in the experimental test-bench of Section 7, while the resistance term is taken as a fraction of the characteristic air impedance $\rho_0 c_0$. This convention follows the one provided in [16]. Hence:

$$\zeta_{Loc}(j\omega) = \frac{1}{\rho_0 c_0} \left(M_d j\omega + R_d + \frac{K_d}{j\omega} \right), \quad (27)$$

Model parameters	M_0	R_0	K_0	Bl/S_e
Units	kg/m ²	Pa.s/m	Pa/m	Pa.A ⁻¹
Values	0.342	133	2.96×10^6	846

Table 1. Model parameters of the ER. The values of R_0 and Bl/S_e are provided for results shown in Sections 6 and 7.

where $R_d = r_d \rho_0 c_0$ is the desired resistance, while the desired reactive components are defined as $M_d = \mu_M M_0$ and $K_d = \mu_K K_0$, with M_0 and K_0 the acoustic mass and stiffness of the open-circuit ER prototype employed in the experimental test-bench of Section 7. Their values are reported in Table 1. The resonance frequency of ζ_{Loc} can be varied by tuning either the stiffness μ_K or the mass μ_M parameters, as $f_d = f_0 \sqrt{\mu_K/\mu_M}$, with f_0 being the resonance frequency of the open-circuit ER (468 Hz). Reducing $\mu_M = \mu_K$, or increasing r_d , allows to reduce the quality factor of the SDOF resonator.

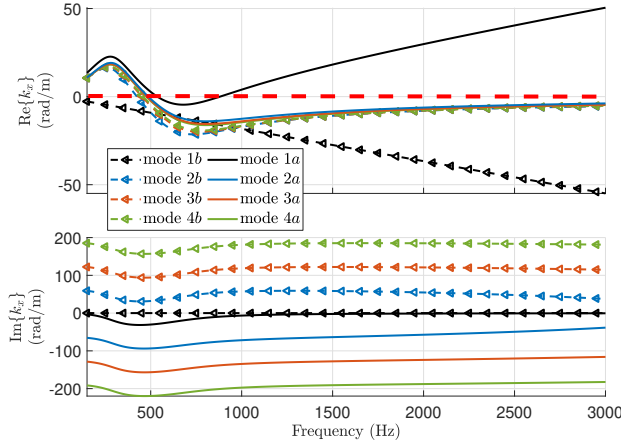
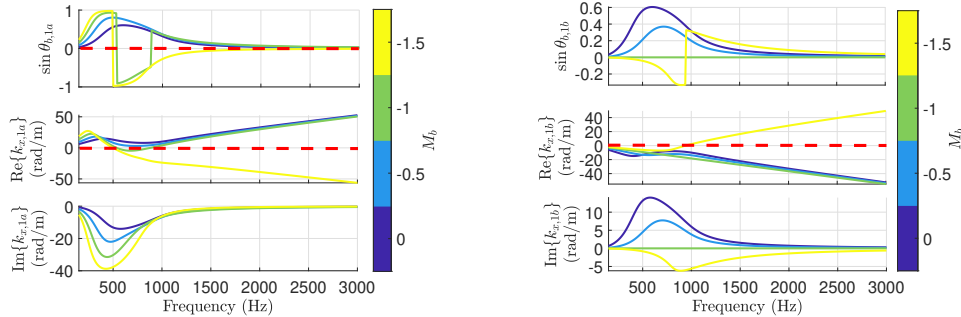


Figure 15. Dispersion plots relative to the first eight duct modes in case of ABL with complex $\zeta_{Loc}(j\omega)$ given by Eq. (27). The control parameters are set to $\mu_M = \mu_K = 0.5$, $r_d = 1$, and $M_b = -1$. In dashed red is the line $\text{Re}\{k_x\} = 0$

Fig. 15 shows the dispersion plots of $k_x(\omega)$ for $\mu_M = \mu_K = 0.5$, $r_d = 1$, and $M_b = -1$. The modes are not labelled referring to their sense of propagation (positive or negative) as the $\text{Re}\{k_x\}$ happens to change its sign with frequency, while sign of $\text{Im}\{k_x\}$ is unaltered. Mode 1b corresponds to the backward propagating plane wave always present for $M_b = -1$. Mode 1a

is the first mode propagating toward $+x$. Nevertheless, $\text{Re}\{k_{x,1a}\}$ becomes 505
negative between approximately 500 and 870 Hz, which means a reverse in 506
the direction of propagation. In such frequency range, $\text{Re}\{k_x\}$ and $\text{Im}\{k_x\}$ 507
present the same sign, which means unstable propagation. Therefore, we can 508
state that, for $\mu_M = \mu_K = 0.5$, $r_d = 1$ and $M_b = -1$, the ABL does not fulfil 509
the modal passivity criteria for any mode, except for mode $1b$. Hence, the 510
absolute passivity conditions $\text{Re}\{\zeta_{Loc}\} \geq 0$ and $|M_b| < 1$, sufficient in case 511
of open-field or purely resistive ζ_{Loc} , will not be sufficient in case of reactive 512
 ζ_{Loc} . As this phenomenon does not happen for purely real ζ_{Loc} (see Section 513
4.1), neither in case of locally-reacting boundary ($M_b = 0$), we expect that 514
the ABL could restore modal passivity by reducing the reactive character of 515
 ζ_{Loc} , or by decreasing M_b . It is interesting to highlight that such non-passive 516
behaviour cannot be detected in open-field, suggesting also the influence of 517
the cross-section dimension in the duct-modes stability. 518

Fig. 16a shows the spectra of $\sin\theta_{b,1a}$ and of the real and imaginary 519
parts of $k_{x,1+}$, with varying $M_b < 0$. Increasing $|M_b|$ leads to higher values 520
of $\text{Im}\{k_{x,1a}\}$ around resonance (as in case of purely resistive ζ_{Loc}). Though, 521
for $M_b = -1$ and -1.5 , the $\text{Re}\{k_{x,1a}\}$ changes its sign in a frequency range 522
starting just above resonance. The higher $|M_b|$, the larger is such frequency 523
band of non-passive behaviour. Indeed, while for $M_b = -1$ passivity is 524
restored at about 900 Hz, in case of $M_b = -1.5$, passivity is never restored in 525
the frequency range under study. It is remarkable the correlation of $\sin\theta_{b,1a}$ 526
with both the acoustical passivity and the attenuation rate. Indeed, the 527
frequency bandwidth where $\text{Re}\{k_{x,1a}\}$ changes its sign, coincides perfectly 528
with the bandwidth where $\sin\theta_{b,1a} < 0$. Moreover, in the passivity regions, 529
 $\sin\theta_{b,1a}$ is higher when $\text{Im}\{k_{x,1a}\}$ presents larger values, thus confirming the 530
correlation with the attenuation rate. In Fig. 16b, the same modal quantities 531
are plotted with varying $M_b < 0$, but for mode $1b$. Notice the plane wave 532
solution for $M_b = -1$. For $M_b = -1.5$, the $\text{Im}\{k_{x,1b}\}$ becomes negative as 533
the $\text{Im}\{k_{x,1-}\}$ in case of purely real ζ_{Loc} (check Fig. 8b). Nevertheless, the 534
 $\text{Re}\{k_{x,1+}\}$ changes its sign, therefore restraining the non-passive behaviour 535
up to about 950 Hz. After this frequency, passivity gets restored. Once again, 536
check the perfect correlation of the dispersion solutions with the values of 537
 $\sin\theta_{b,1b}$, both in terms of passive bandwidth and attenuation rates. Fig. 17 538
shows the effect of the quality factor of ζ_{Loc} upon the modal quantities of 539
mode $1a$, for $M_b = -1$. In particular, Fig. 17a shows the effect of the reactive 540
terms $\mu_M = \mu_K$, while Fig. 17b shows the effect of the resistive one r_d . As 541
expected, by reducing the quality factor of ζ_{Loc} (by decreasing $\mu_M = \mu_K$ 542
and/or augmenting r_d), we can restore the acoustical passivity. Once again, 543
both passivity limits and attenuation rates are perfectly captured by $\sin\theta_{b,1a}$. 544

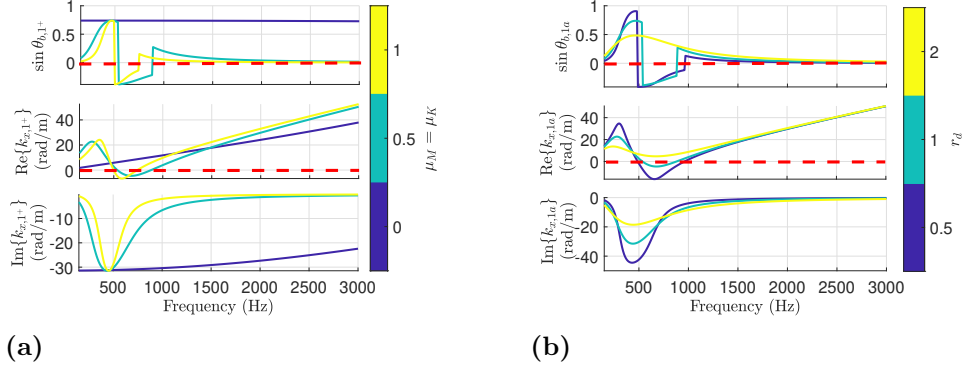


(a) (b)
Figure 16. Spectra of $\sin \theta_{b,m}$, real and imaginary parts of $k_{x,m}$, for mode 1a (a) or 1b (b), with M_b varying. The other parameters are set to $\mu_M = \mu_K = 0.5$, $r_d = 1$, and the duct cross section width is $h = 0.05$ m. The dashed red lines separate passive and non passive conditions.

Finally, we want to check the effect of the duct cross-section width h . In Fig. 18, h is halved and doubled with respect to the default value, demonstrating that such non-passive behaviour is strictly related to the duct cross-section size. The narrower the duct cross-section is, the larger is the bandwidth of passivity loss. It is also interesting to remark that $\sin \theta_{b,1a}$, despite perfectly capturing the frequency ranges of non-passive behaviour, is not able to capture the variation of attenuation level ($\text{Im}\{k_{x,1a}\}$) with h . It looks like the boundary modal group velocity (which gives $\sin \theta_{b,1a}$) is not informed by the variation of the duct cross section size, except if h leads to a change of direction of propagation. A deeper analysis of the modal group velocity \vec{c}_m on the boundary, and the effect of h upon it, is out of the scope of the present paper, but it will be retrieved in a future study. Nevertheless, as h is not a parameter related to the boundary operator, the quantity $\sin \theta_{b,m}$ can still be employed for liner optimization purposes.

Below, the main outcomes of Section 4:

- In case of purely real ζ_{Loc} , the ABL absolute passivity limits in duct grazing incidence, coincide with the passivity limits in open field.
- For $|M_b| > 1$, modal passivity is lost for the first mode propagating in the same direction as M_b , while it is preserved for duct modes propagating against M_b .



(a) (b)
Figure 17. Spectra of $\sin \theta_{b,m}$, real and imaginary parts of $k_{x,m}$, for mode 1a, with varying $\mu_M = \mu_K$ (a) or r_d (b). The default parameters are set to $\mu_M = \mu_K = 0.5$, $r_d = 1$, $M_b = -1$, and the duct cross section width is $h = 0.05$ m. The dashed red lines separate passive and non passive conditions.

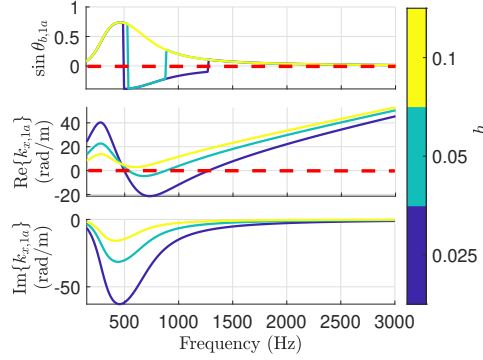


Figure 18. Spectra of $\sin \theta_{b,m}$, real and imaginary parts of $k_{x,m}$, for mode 1a, with varying h . The control parameters are set to $\mu_M = \mu_K = 0.5$, $r_d = 1$ and $M_b = -1$. The dashed red lines separate passive and non passive conditions.

- The ABL boundary convection increases $\sin \theta_{b,m}$ for modes propagating against M_b , analogously to air-flow convection which increases the modal propagation angle of upstream propagating modes [47].
- In case of complex ζ_{Loc} , the open field passivity criteria do not coincide with the absolute passivity conditions in grazing incidence.
- In case of complex ζ_{Loc} , mode 1a passivity is reduced when:

the quality factor of ζ_{Loc} increases, $|M_b|$ augments, and the duct cross-section width is reduced.

- $\sin \theta_{b,m}$ provides a criteria for both passivity and attenuation rates, both in case of purely real and complex ζ_{Loc} .
- Non-reciprocal propagation is evident by the first duct-mode solutions: mode 1^+ (read $1a$ for complex ζ_{Loc}) is attenuated, while mode 1^- (read $1b$ for complex ζ_{Loc}) is a plane wave, for $M_b = -1$ and independently from ζ_{Loc} .

5 Scattering simulations in 2D waveguide

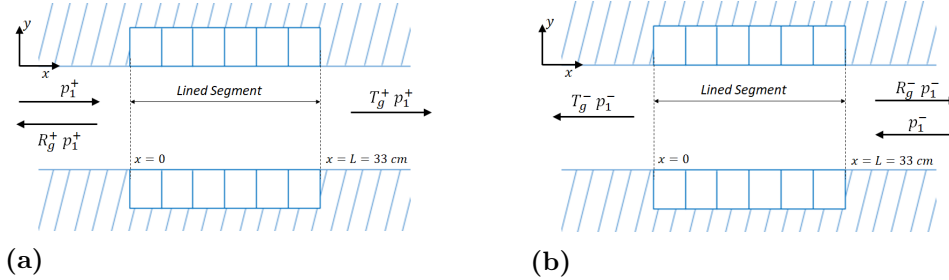


Figure 19. Lining segment and scattering coefficients definition in a 2D waveguide lined on both sides.

In this section the ABL is analysed in terms of scattering performances in the plane wave regime. The liner is considered to extend for an axial length $L = 0.3$ m in a 2D acoustic waveguide of cross-section height $h = 0.05$ m, without flow. Such dimensions correspond to the experimental setup that will be presented in Section 7. The scattering problem is illustrated in Fig. 19, where the reflection R_g and transmission T_g coefficients are defined for incident field directed toward either $+x$ or $-x$. The subscript g is employed to differentiate the present *grazing* incidence from the oblique incidence scattering of Section 3. The ABL is applied continuously on the boundary of the waveguide in the lined segment. The scattering matrix is defined in Eq. (28) for the plane wave regime of a hard-walled duct.

$$\begin{bmatrix} p_2^+ \\ p_1^- \end{bmatrix} = \begin{bmatrix} T_g^+ & R_g^- \\ R_g^+ & T_g^- \end{bmatrix} \begin{bmatrix} p_1^+ \\ p_2^- \end{bmatrix}. \quad (28)$$

The superscript signs $+$ or $-$ in Eq. (28), indicate the direction of propagation of the incident plane wave (toward either $+x$ or $-x$). The

results in terms of scattering matrix coefficients, have been obtained by FE 597
simulations in Comsol. As in the duct mode analysis, the FE mesh has 598
been built sufficiently fine to fully resolve both longitudinal and transversal 599
pressure field up to $f_{max} = 3$ kHz. The scattering coefficients T_g^\pm and R_g^\pm 600
are computed, by exciting first the left and then the right termination. In 601
the scattering problem, high noise isolation toward $+x$ ($-x$) corresponds to 602
low values of T_g^+ (T_g^-). The acoustical passivity, in the plane wave regime, 603
corresponds to positive values of both α_g^+ and α_g^- . 604
As in the duct mode analysis, we differentiate the case of purely real or 605
resonant ζ_{Loc} in the ABL. 606

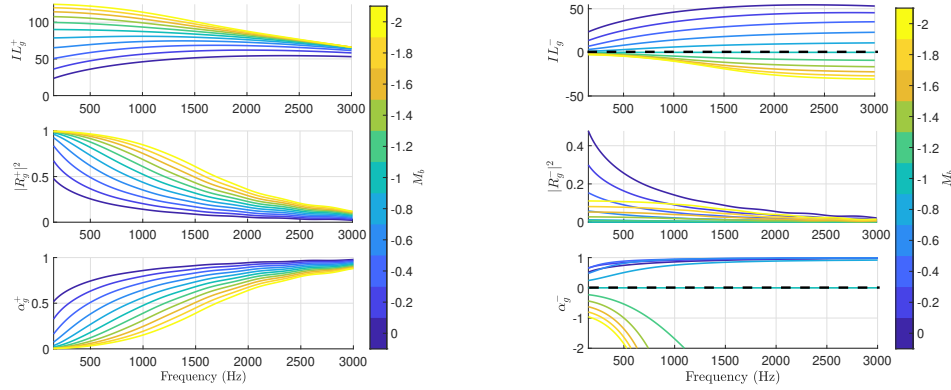
5.1 Real local impedance ζ_{Loc} 607

The scattering performances are presented in terms of power scattering 608
coefficients for both positive and negative propagation. The power scattering 609
coefficients are defined from the power balance [38] which, in case of plane 610
waves, reduces to: 611

$$1 = \alpha_g^\pm + |T_g^\pm|^2 + |R_g^\pm|^2, \quad (29)$$

where R_g and α_g are the reflection and absorption coefficients in graz- 612
ing incidence, respectively. From $|T_g^\pm|^2$, it is possible to compute the 613
Transmission Loss $(TL_g^\pm)_{Liner} = 10 \log_{10}(1/|T_g^\pm|^2)$, and the Insertion Loss 614
 $IL_g^\pm = (TL_g^\pm)_{Liner} - (TL^\pm)_{Rigid}$. As $(TL^\pm)_{Rigid} = 0$ in simulations, $IL^\pm =$ 615
 $(TL_g^\pm)_{Liner}$. 616

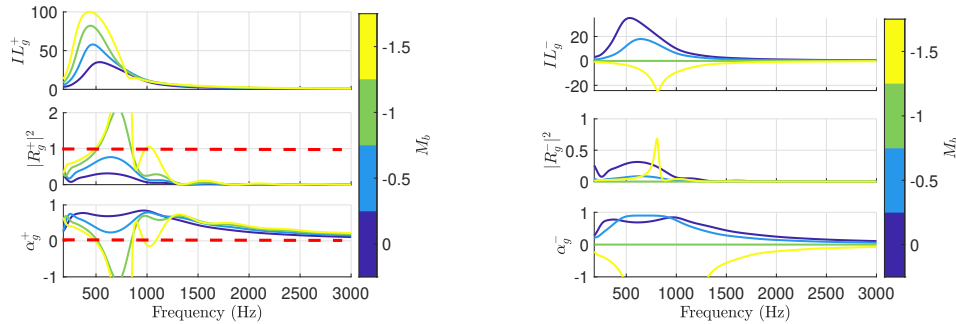
Fig. 20a shows the power scattering coefficients in case of $\zeta_{Loc} = 1$, for 617
 M_b continuously varying from 0 to -2 . Coherently with the duct mode 1^+ 618
solution reported in Section 4.1, increasing the absolute value of $M_b < 0$, 619
brings about an increase in the IL_g^+ , especially at low frequencies. Observe 620
that such increase of IL_g^+ is accompanied by a significant increment of the 621
back-reflection and, less intuitively, by a reduction of absorption. This means 622
that, in such configuration of waveguide with both upper and lower sides 623
lined by the ABL, excited by plane waves propagating against the boundary 624
advection speed, most energy is reflected back rather being absorbed. In case 625
of negative propagation, i.e. plane waves propagating concordant with M_b , 626
perfect transmission is assured for $M_b = -1$, while for $M_b < -1$, the loss of 627
passivity ($\alpha_g^{-1} < 0$) of the ABL manifests itself by $|T_g^-| > 1$ in agreement 628
with the change of sign of $\text{Im}\{k_{x,1^+}\}$ showed in Fig. 8b. The passivity 629
limits are highlighted by dashed black line in Fig. 20. These results are 630
totally coherent with the results of Section 4.1 both in terms of attenuation 631
performances and passivity. Moreover, perfect non-reciprocal propagation is 632



(a) (b)
Figure 20. Scattering coefficients in a 2D waveguide of cross section width $h = 0.05$ m with lined segment of length $L = 0.3$ m, lined on both sides by the boundary advection law with $\zeta_{Loc} = 1$, and varying M_b .

achieved for $M_b = -1$, as $IL_g^- = 0$, while IL_g^+ is very high. This, also, is in 633
agreement with the dispersion solutions of Section 4.1. 634

5.2 Complex local impedance ζ_{Loc} 635



(a) (b)
Figure 21. Scattering coefficients for excitation coming from the left (a) or right (b) termination, in a 2D waveguide of cross section height $h = 0.05$ m with lined segment length $L = 0.3$ m, and ABL applied on both sides of the duct, with $\mu_M = \mu_K = 0.5$, $r_d = 1$ and varying M_b .

As in Section 4.2, we consider here the scattering problem in case of 636
 ζ_{Loc} assuming the SDOF resonator form of Eq. (27), with default mass 637

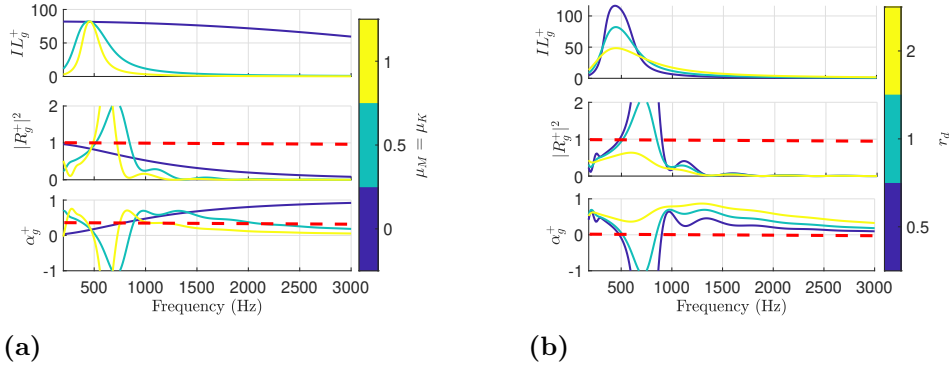


Figure 22. Scattering coefficients for excitation coming from the left, in a 2D waveguide of cross section width $h = 0.05$ m with an ABL lining both sides for an extension of $L = 0.3$ m, in case of $M_b = -1$, and with varying $\mu_M = \mu_K$ **(a)**, or varying r_d **(b)**. The default values are $\mu_M = \mu_K = 0.5$ and $r_d = 1$.

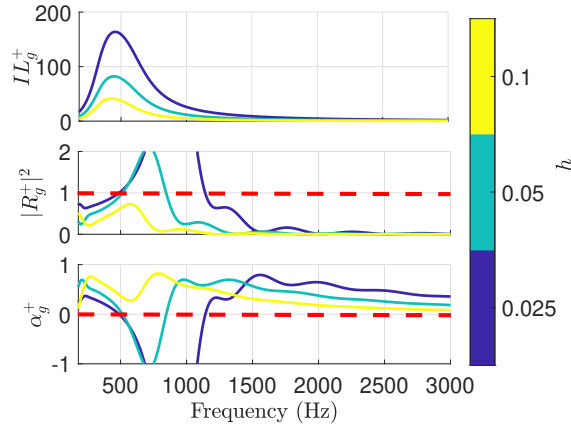


Figure 23. Scattering coefficients in a 2D waveguide of variable cross section width h , lined segment of length $L = 0.3$ m, lined on both sides by the ABL with $M_b = -1$, $R_d = \rho_0 c_0$ and $\mu_M = \mu_K = 0.5$.

and stiffness coefficients $\mu_M = \mu_K = 0.5$, and resistance term $r_d = 1$. Fig. 638
 21a shows the effect of varying M_b in case of incoming field from the left 639
 duct termination, indicated by + superscript. As expected, increasing the 640
 absolute value of $M_b < 0$, improves isolation (augments IL_g^+). But, after 641
 the resonance of ζ_{Loc} , α_g^+ becomes negative for $M_b = -1$, up to about 642
 870 Hz. This loss of passivity corresponds to a reflection coefficient higher 643
 than 1, in agreement with the change of sign of $\text{Re}\{k_{x,1a}\}$ in Fig. 16a, 644

which becomes negative at about 500 Hz, and comes back to be positive
 at about 870 Hz. Notice the interesting correlation between an unstable
 propagation of mode $1a$ toward $-x$ in the range 500 – 870 Hz, and the
 reflection coefficient higher than 1 in the same frequency range. Since the
 duct mode instability manifests as a *backward* propagation, this translates
 into higher acoustic energy reflected *backward*. Also for $M_b = -1.5$ in Fig.
 16a, we have non-passive behaviour, as expected, corresponding once again to
 a $|R_g^+| > 1$. Nevertheless, passivity is restored around 870 Hz, then lost again
 in a narrow bandwidth around 1000 Hz, and definitively retrieved till 3 kHz.
 This behaviour is not simply related to the duct mode $1a$ solution, which, in
 fact, shows unstable propagation from 500 till 3 kHz, in case of $M_b = -1.5$.
 Indeed, both modes $1a$ and $1b$ participate in the scattering problem. In
 particular, mode $1b$ (check Fig. 16b) restores its passivity around 950 Hz. In
 order to fully identify the participation of duct modes solutions $1a$ and $1b$ (as
 well as of higher order modes), a mode-matching analysis will be carried out
 in a future dedicated study, where all duct-mode solutions will be correlated
 to a multi-modal scattering problem. In case of $M_b = -1$ instead, mode
 $1b$ is always a plane wave (stable), therefore it does not affect the passivity
 of the ABL. Figs 22 and 23 show the effect of varying the quality factor
 and the duct cross section width, respectively. The advection speed is fixed
 with $M_b = -1$, hence, as said before, only the duct mode $1a$ is impacting
 the passivity in the scattering solution. Indeed, the scattering coefficients
 of Figs 22 and 23 perfectly correlate with the modal plots of Figs 17 and
 18, with the loss of passivity confined in a bandwidth starting above ζ_{Loc}
 resonance. Fig. 22 confirms that by reducing the quality factor (decreasing
 $\mu_M = \mu_K$ or augmenting r_d) we can restore the acoustical passivity of the
 ABL in grazing incidence. Therefore, for any duct cross-section width, the
 scattering solutions confirm the outcomes of modal analysis, according to
 which it should always be possible to have a passive behaviour of the ABL
 in the frequency range of interest (here the plane wave regime of the rigid
 waveguide) by either reducing M_b or the quality factor.
 Remark that, in the plane wave regime of the hard-walled duct, the scattering
 solutions give no information about the energy exchanged with higher order
 rigid-duct modes. Indeed, those latter ones are not able to propagate along
 the rigid-duct segments preceding and following the liner. Therefore, an
 apparent passive behaviour of the scattering coefficients in the plane wave
 regime, is not correlated to an *absolute passivity* as it is defined in Eq. (25).
 Indeed, in order to assess absolute passivity from scattering solutions, we
 should solve the scattering problem at all frequencies. In the case study
 reported in this paper, the passive behaviour featured by the ABL in the

plane wave regime, is actually related to the *modal* passivity defined in Eq. (26), relative to modes 1a and 1b. Therefore, in order to assure no amplification of propagated energy in the frequency range of interest, the *modal* passivity criteria defined in Eq. (26) plays an important role. We finally invite the reader to remark that the loss of acoustical passivity always concerns propagation (either forward transmission or backward reflection) in the same direction as M_b . This is so, in the open field case of Section 3, in the duct mode analysis of Section 4, and in the scattering solution of the present Section.

- In case of purely real ζ_{Loc} , the scattering coefficients perfectly correlate with the duct mode solutions 1^+ and 1^- , in terms of isolation performances, modal passivity and non-reciprocal propagation.
- The enhancement of isolation performances induced by the ABL, for excitation field propagating against M_b , manifests itself with higher backward reflection, in case of ABL lining both upper and lower sides of the duct.
- In case of complex ζ_{Loc} , we have good correlation between the first duct-mode solutions and the scattering coefficients. Nevertheless, because of the change of sign the first duct-mode solutions, a proper mode-matching analysis is needed to perfectly capture the participation of each mode in the scattering performances.
- In case of complex ζ_{Loc} , the loss of acoustical passivity related to a reversed direction of duct-mode propagation (change of sign of $\text{Re}\{k_x\}$), corresponds to a backward reflection coefficient higher than 1. The unstable propagation always happens in the same sense as M_b .
- The scattering coefficients confirm the non-reciprocal propagation for $|M_b| = 1$.

6 Scattering simulations in 3D waveguide

In this section we simulate the scattering performances in the plane wave regime of a 3D acoustic waveguide, of square cross section with 5 cm lateral sides, without flow. The ABL is applied along each side of the duct for a

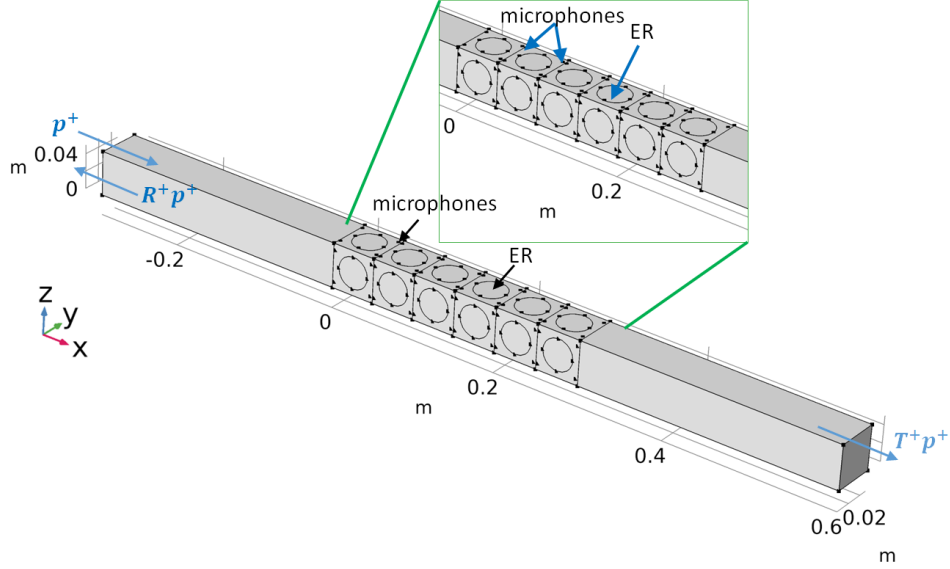


Figure 24. 3D geometry for scattering simulations, in case of ERs disks applied flush on the duct boundary.

length of 30 cm. In order to investigate the effect of discretizing the ABL by individual ERs lining the parietal walls of a rectangular cross section duct, as in the experimental test-rig of Section 7, the ABL is applied on separate disks of diameter 3.6 cm, simulating the ERs (6 per each duct edge), as shown in Fig. 24. The dynamics of each speaker is simulated according to the Thiele-Small SDOF model [50].

The loudspeaker model is reported in Eq. (30), in terms of the Laplace variable s :

$$Z_0(s)\bar{v}(s) = \bar{p}(s) - \frac{Bl}{S_e}\bar{i}(s). \quad (30)$$

In Eq. (30), $\bar{p}(s)$ and $\bar{v}(s)$ are the acoustic pressure and velocity, respectively, on the speaker diaphragm, $\bar{i}(s)$ is the electrical current in the speaker coil, $Z_0(s) = M_0s + R_0 + K_0/s$ is the acoustical impedance of the loudspeaker in open circuit, with M_0 , R_0 and K_0 the corresponding acoustical mass, resistance and stiffness. The electrical current $\bar{i}(s)$ is multiplied by the force factor Bl to get the electromagnetic force, and divided by the effective area S_e to retrieve an equivalent pressure. Observe that the impedance description of Eq. 30 is a lumped-element model, which is reliable as long as the wavelength of the acoustic field is sufficiently larger than the size

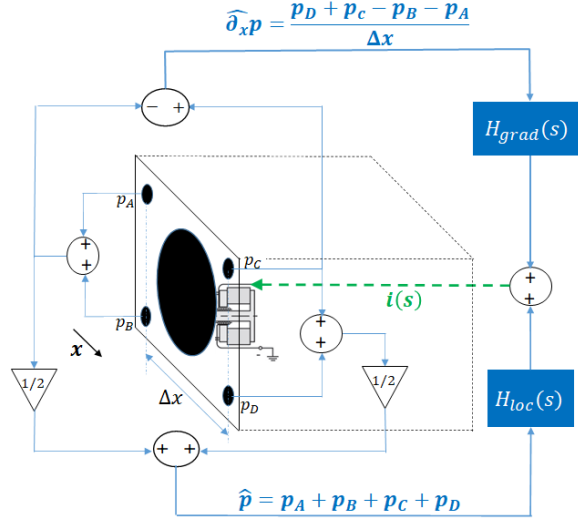


Figure 25. Sketch of the 4-microphones ER control, corresponding to Eq. (31).

of the speaker diaphragm. This is true for any local impedance modelling. 736
 The upper frequency of validity of the lumped-element assumption is much 737
 beyond the frequency range of validity of the SDOF loudspeaker-model, 738
 which lies around the first speaker mode (around 468 Hz). Therefore, both 739
 the lumped-element assumption and the SDOF model are valid around the 740
 principal resonance of the ER. 741

The ABL is implemented by defining the electrical current $i(s)$ as in Eq. 742
 (31): 743

$$i(s) = H_{loc}(s)\hat{p}(s) + H_{grad}(s)\hat{\partial}_x\bar{p}(s), \quad (31)$$

where $\hat{p}(s)$ and $\hat{\partial}_x\bar{p}(s)$ are the estimated local pressure and its x-derivative 744
 on each speaker diaphragm, in the Laplace domain. The local sound pressure 745
 is estimated by averaging the four microphones on the corners of each 746
 ER $\hat{p} = (p_A + p_B + p_C + p_D)/4$, while the x-derivative is estimated by a 747
 first-order finite difference $\hat{\partial}_x\bar{p} = \left((p_C + p_D) - (p_A + p_B) \right) / \Delta x$, with $\Delta x \approx 4$ 748
 cm the distance between the microphones before (A,B) and after (C,D) each 749
 ER speaker, along the x-direction, as showed in Fig. 25. A time delay of 750
 $\tau = 2 \times 10^{-5}$ seconds between the pressure inputs and the electrical current, 751
 is considered by multiplying the microphones pressures by $e^{-j\omega\tau}$, in order to 752
 simulate the physiological latency of the digital control algorithm of the ER 753

[16].

The transfer functions $H_{loc}(s)$ and $H_{grad}(s)$ are defined based upon the loudspeaker model of Eq. (30). Equating the velocity of the speaker diaphragm from Eq. (30), and the velocity corresponding to the ABL (Eq. (8)), we get the expressions in the Laplace space of H_{loc} and H_{grad} , in Eq.s (32) and (33), respectively.

$$H_{loc}(s) = \frac{S_e}{Bl} \left(1 - \frac{Z_0(s)}{Z_{Loc}(s)} \right), \quad (32)$$

$$H_{grad}(s) = -\frac{S_e}{Bl} \frac{Z_0(s)}{Z_{Loc}(s)} \frac{U_b}{s} F_{hp}(s), \quad (33)$$

where $F_{hp}(s)$ in $H_{grad}(s)$ is a high-pass filter necessary in order for $H_{grad}(j\omega)$ not to become infinite for $\omega \rightarrow 0$. Notice also, that a purely real Z_{Loc} would lead to non-causal H_{loc} and H_{grad} , therefore we have employed the SDOF expression of Eq. (27) for Z_{Loc} (as in Sections 4.2 and 5.2) in the correctors H_{loc} and H_{grad} . The synthesis of our corrector transfer functions, is also called *model inversion* [51] approach, as the objective of the controller is to cancel out the loudspeaker proper dynamics, and replace it with a desired acoustic behaviour. Both H_{loc} and H_{grad} depends upon the loudspeaker own impedance model Z_0 . Therefore, each parameter appearing in Eq. (30) must be estimated. The so-called Thiele-Small parameters are identified by acoustic measurements, as described in [52], and their values are reported in Table 1. Further details upon such control strategy can be found in [16, 23].

Both Eq.s (32) and (33) are implemented in the Comsol model. From the microphones estimation of \hat{p} and $\hat{\partial}_x p$, the electrical current i is obtained from Eq. (31). Hence, the loudspeaker dynamics Eq. (30) is solved for $\bar{v}(s)$, which is then imposed on the disks representing the speaker membranes in the numerical model.

It is worthy to note that the control filters presented here in Eq.s (32) and (33) target a resonant Z_{Loc} , while in references [27] and [28], Z_{Loc} was considered as just a mass term, limiting its applicability to frequencies above the loudspeaker resonance.

The model showed in Fig. 24 is solved for the scattering coefficients as in Section 5. The FE mesh elements have the same maximum size as those in Section 5.

In Fig. 26a, the scattering coefficients achieved by the ABL with $M_b = -1$, are plotted along with the ones relative to local impedance control ($M_b = 0$),

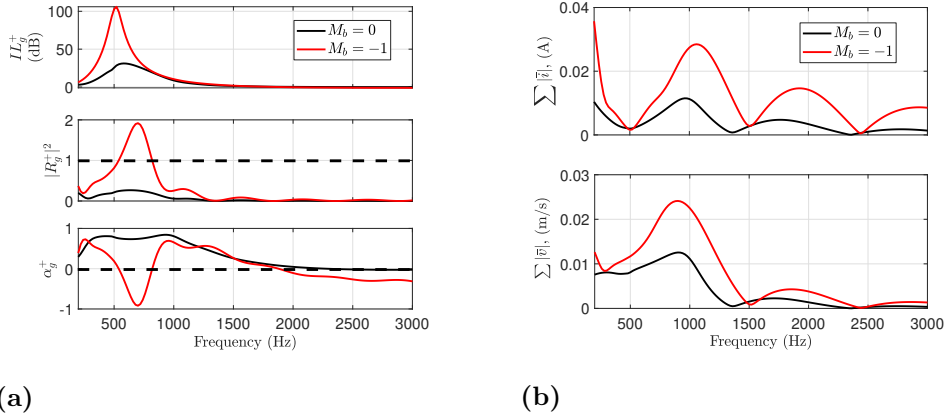


Figure 26. Comparison between local impedance control ($M_b = 0$) and ABL ($M_b = -1$), in terms of scattering coefficients in the 3D waveguide **(a)**, and in terms of sum of all ERs electrical current spectra $\sum |\bar{i}|$ and velocity spectra $\sum |\bar{v}|$ **(b)**.

applied on each ER. The ζ_{Loc} parameters are set to $\mu_M = \mu_K = 0.5$ and $R_d = \rho_0 c_0$. As in the 2D case, the ABL demonstrates higher isolation capabilities, though being non-passive slightly after resonance. Notice also the loss of passivity at high frequencies (above 2 kHz), which was not predicted by the 2D simulations. This is mostly due to the time delay [16]. In Appendix B, we briefly check the effects of the finite difference approximation of $\partial_x p$ and of time delay. In Fig. 26b, the electrical current spectra of all the ERs are summed up to visualize how the ABL requires a much higher level of electrical current (up to 3 times at some frequencies) with respect to the local impedance control. Also the sum of velocities on the 24 ERs is reported showing once again higher vibrational amplitudes required by the ABL.

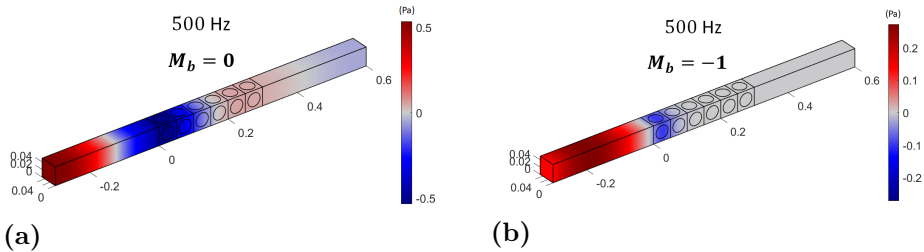


Figure 27. 3D surface plots of the sound pressure field at 500 Hz, in case of local impedance control **(a)** or ABL with $M_b = -1$ **(b)**, on the ERs.

Fig. 27 compares the sound field at 500 Hz computed in the duct for an incident pressure of 1 Pa, when local impedance control (Fig. 27a) or ABL (Fig. 27b) is applied on the ERs. Observe how the sound pressure field gets annihilated as soon as it enters the segment lined by the ABL. The enhancement of sound transmission attenuation for $M_b = -1$, with respect to the case of $M_b = 0$, is unequivocal.

7 Experimental results

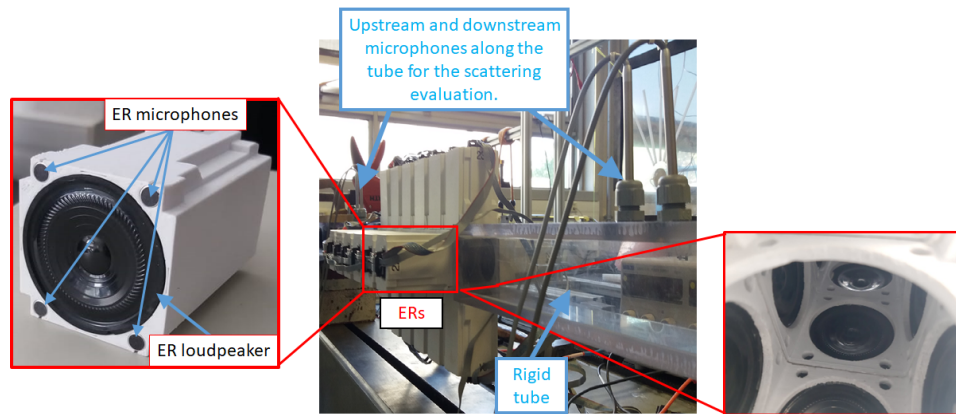


Figure 28. ER prototype (left); waveguide (middle) for the scattering evaluation, with internal view of the lined segment (right).

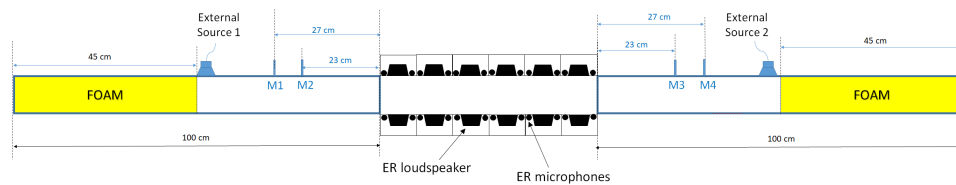


Figure 29. Sketch of the test-bench.

In this section, the advection control law is experimentally tested on an array of 24 ER prototypes lining a squared cross-section duct of about 0.05 m side, as illustrated in the photos of Fig. 28 and in the sketch of Fig. 29. The ERs are placed 6 per each side of the duct, as showed in Fig. 28. Each ER has a surface area of about $0.05 \times 0.05 \text{ m}^2$, for a total lined segment length of about 0.3 m in the duct. Both ends of the tube are filled with 45

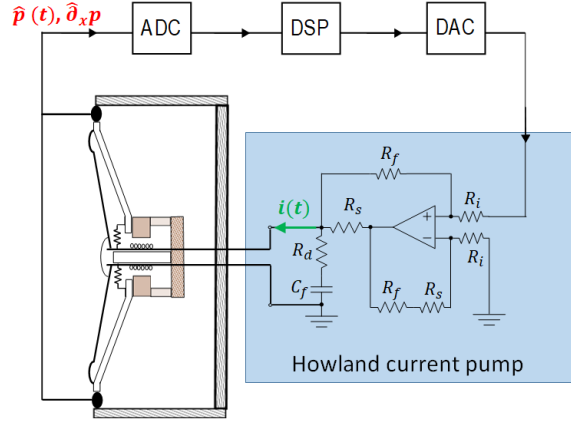


Figure 30. Sketch of the ER architecture.

cm of foam to reproduce quasi-anechoic conditions at the input and output 814
of the waveguide. An external acoustic source is placed flush with the duct 815
surface on both sides of the waveguide, just ahead of the foam terminations, 816
sufficiently far from the lined segment and from microphone locations. The 817
external sources are excited with a sine-sweep signal from 150 Hz (lower limit 818
of the source-loudspeakers) to 3 kHz (to stay below the cut-on frequency of 819
the higher rigid duct modes). 820

Each ER is controlled autonomously, and the control architecture is illustrated 821
in Fig. 30: the signals \hat{p} and $\hat{\partial}_x p$ on the speaker diaphragm, after being 822
digitally converted by the Analogue-Digital-Converter (ADC), are fed into a 823
programmable digital signal processor (DSP) where the output of the control 824
is computed at each time step. The Howland current pump [53] allows to 825
enforce the electrical current i in the speaker coil independently of the voltage 826
at the loudspeaker terminals. It consists of an operational amplifier, two 827
input resistors R_i , two feedback resistors R_f , and a current sense resistor R_s . 828
The resistance R_d and capacitance C_f constitutes the compensation circuit 829
to ensure stability with the grounded load [54]. More details can be found in 830
[16]. 831

All ERs and control interfaces have been produced in the Department of 832
Applied Mechanics at FEMTO-st Institute. The control laws have already 833
been defined in Section 6, by Eq. (31), (32), (33), and the loudspeaker 834
parameters provided in Table 1. The four scattering coefficients have been 835
estimated according to the two-source method [49]. 836

In Fig. 31, the IL_g^+ from measurement is compared to the one obtained 837
from 3D simulations (given in Section 6), for $\mu_M = \mu_K = 0.5$, $R_d = \rho_0 c_0$ 838

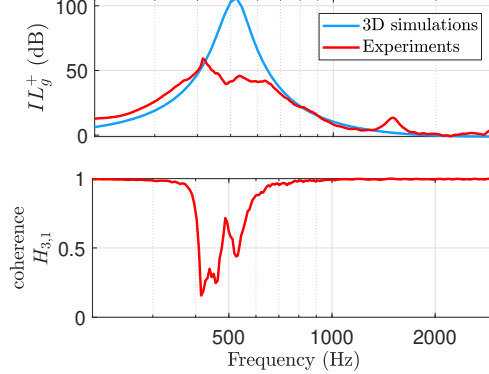
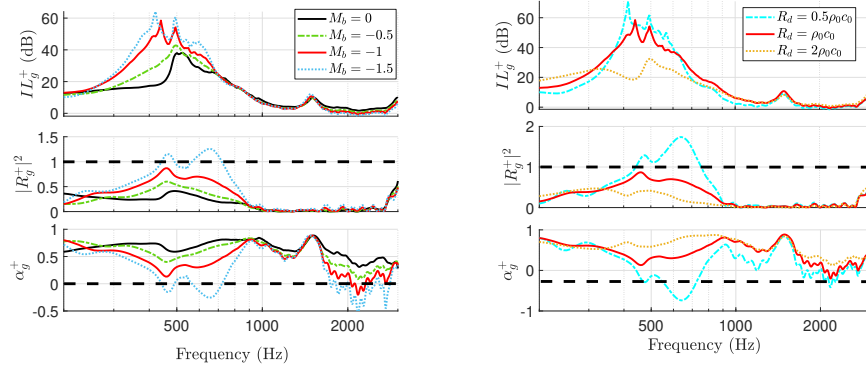


Figure 31. Comparison between measurements (in red) and simulations (in blue) for ABL with $\mu_M = \mu_K = 0.5$, $R_d = \rho_0 c_0$ and $M_b = -1$.

and $M_b = -1$. Observe how, despite the inevitable model uncertainties, 839
the trends before and after the resonance peak are well captured by the 840
3D simulations, except around 1.5 kHz where an additional speaker mode 841
appears, as in [16]. The peak of more than 100 dB of attenuation predicted 842
by the simulations, is not visible experimentally. This is indeed due to the 843
very low signal-to-noise ratio at microphone 3 caused by the extreme isolation 844
accomplished by the ABL. This prevents the detection of very high IL values, 845
as confirmed by the low level of coherence around resonance, of the transfer 846
functions between microphones on opposite sides with respect to the lined 847
segment (check the coherence of transfer function $H_{3,1}$ between microphones 848
3 and 1, in Fig. 31). 849

Fig. 32a and 32b show the experimental scattering coefficients for incident 850
field toward $+x$, with varying M_b and R_d respectively. The default parameters 851
are set to $\mu_M = \mu_K = 0.5$, $R_d = \rho_0 c_0$ and $M_b = -1$. Fig. 32a confirms the 852
higher isolation achieved by increasing the absolute value of $M_b < 0$, though 853
the IL_g^+ for $M_b = -1.5$ does not look significantly augmented with respect to 854
 $M_b = -1$. This, once again, can be explained by an excessively low signal-to- 855
noise ratio of microphones after the lined segment (microphones 3 and 4 for 856
positive propagation), and the consequent low coherence of the corresponding 857
transfer function. The reflection and absorption coefficients though, are still 858
able to follow the expected trends, with the loss of passivity immediately after 859
resonance. Fig. 32b also validates the numerical predictions both in terms of 860
isolation performances and passivity, demonstrating that increasing the 861
quality factor brings about an excess in the backward reflection, endangering 862



(a) **(b)**
Figure 32. Experimental scattering performances for incident field propagating toward $+x$, achieved by the ABL with varying M_b (a), or varying R_d . The default parameters are set to $\mu_M = \mu_K = 0.5$, $R_d = \rho_0 c_0$ and $M_b = -1$.

passivity above resonance. Observe, in Fig. 32a, the reduction of passivity 863
from 1.8 kHz and above with higher $|M_b|$. This is due to a combined effect of 864
time delay and the first order approximation of $\hat{\partial}_x p$, which is clearly amplified 865
for higher values of $|M_b|$. 866

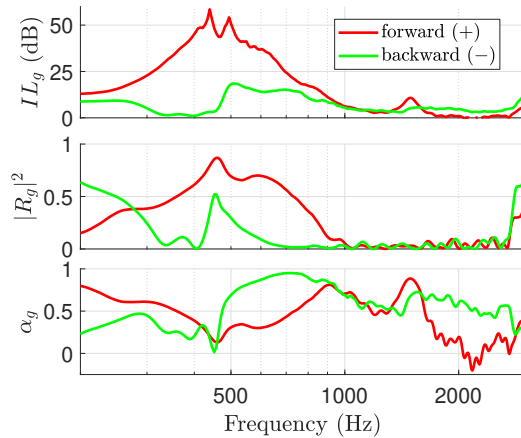


Figure 33. Scattering performances relative to external incident field propagating toward $+x$ (“forward”, in solid red) compared to the ones relative to “backward” incident field (in solid green), in case of ABL with $\mu_M = \mu_K = 0.5$, $R_{at} = \rho_0 c_0$ and $M_b = -1$.

The broadband non-reciprocal character of the advective BC is evident by 867
looking at Fig. 33, where the “forward” scattering coefficients (corresponding 868

to the first column of the scattering matrix of Eq. (28)), are plotted along 869
with the “backward” scattering coefficients (corresponding to the second col- 870
umn of the scattering matrix of Eq. (28)), in case of $\mu_M = \mu_K = 0.5$, $r_d = 1$ 871
and $M_b = -1$. Observe that, in the backward direction, we do not have 872
perfect transmission. Indeed, because of time-delay and model-uncertainties 873
in the actual control system, the model-based correctors H_{loc} and H_{grad} of 874
Eq. (32) and (33) are not capable to fully cancel out the actuator dynamics, 875
leading to residual non-zero loudspeaker response and non-perfect transmis- 876
sion in the backward direction. Further details on the limitation of such 877
corrector synthesis approach can be found in [16]. Nevertheless, IL_g^- never 878
overcomes 18 dB, while for forward propagation IL_g^+ is significantly higher 879
than 25 dB from 300 to 700 Hz, and higher than 50 dB close to resonance. 880
Notice that such non-reciprocal propagation is achieved in the bandwidth 881
of ζ_{Loc} , while in [28] it was accomplished only above resonance. This is due 882
to the different definitions of H_{loc} and H_{grad} , which are here targeting the 883
frequency range around ζ_{Loc} resonance, allowing to significantly enhance 884
both isolation and non-reciprocal performances in the target bandwidth. 885

Below, the main outcomes of Sections 6 and 7. 886
887

- **The corrector transfer functions are synthesized based upon 888
the model-inversion strategy.** 889
- **The ABL is enforced by estimating the average and the first 890
 x -derivative of p , on each ER.** 891
- **The 3D scattering simulations confirm higher isolation capa- 892
bilities of the ABL with respect to local impedance operators.** 893
- **The experimental implementation also confirms the expected 894
results, in terms of isolation, passivity and non-reciprocal
propagation.** 895
896
- **The physiological time-delay in the digital implementation of 897
the control, endangers high-frequency passivity.** 898

8 Conclusions 899

In this article we have provided a detailed discussion of the Advection Bound- 900
ary Law, which is composed of a local impedance component and a convective 901
term. Starting from its theoretical conception of Section 2, such operator is 902

defined, for the first time, as a degeneration of a Dirichlet-to-Neumann map- 903
 ping of a semi-infinite non-isotropic propagative domain, on the boundary. 904
 As the surface impedance operator can be seen as a special case of Advection 905
 Boundary Law, the general framework originally employed by Morse [35] to 906
 introduce the surface impedance concept, is here retrieved and generalized 907
 to include our advective boundary operator. The semi-infinite approach 908
 naturally leads to the open-field scattering problem and the corresponding 909
 reflection coefficient formula (Section 3). The open-field solution allows the 910
 definition of acoustical passivity in open field which, in case of our Advection 911
 Boundary Operator, depends upon the incidence angle. Following a step- 912
 by-step increase in complexity, we discuss the duct-mode solutions in a 2D 913
 waveguide without flow in Section 4. In particular, we first analyse the case of 914
 purely real local impedance term (Section 4.1), and then the case of complex 915
 local impedance term (Section 4.2). The duct mode analysis leads to the 916
 distinction between *absolute* and *modal* passivity. In case of purely real local 917
 impedance, the passivity limits in open-field assure the absolute passivity 918
 in grazing incidence. Nevertheless, in case of reactive local impedance, the 919
 passivity limits in open-field do not assure absolute passivity in grazing 920
 incidence. In particular, for a boundary advection speed against the incident 921
 field, modal passivity is affected by both the reactive component of the local 922
 impedance, and the boundary advection speed. Moreover, such impact is 923
 stronger for narrower ducts. Nevertheless, for any duct-cross section sizes, it 924
 is always possible to restore stability of the duct-modes of interest, i.e. to 925
 assure the corresponding *modal* acoustical passivity of our Advection Bound- 926
 ary Law. The 2D duct-mode analysis is followed by the resolution of the 927
 2D scattering problem. The correlation between the two studies is evident, 928
 in terms of passivity, attenuation levels and non-reciprocal propagation. A 929
 future study will be dedicated to the resolution of the scattering problem by 930
 mode-matching techniques, allowing to visualize numerically the correlation 931
 between modal and scattering solutions. 932
 In order to guarantee no amplification of propagated energy in the frequency 933
 range of interest, the modal passivity plays an important role. In this paper, 934
 we have provided a physical quantity able to assess both acoustical passivity 935
 limits and attenuation levels, in Section 4. It is the sine of the elevation 936
 angle of modal local group velocity at the boundary. Such quantity can be 937
 employed for liner optimization purposes. Moreover, its nice physical inter- 938
 pretation, allows to clarify the mechanism leading to enhanced attenuation 939
 achieved by the Advection Boundary Law, and should be taken into account 940
 for the design of next generation liners. 941
 The final step of complexity in the numerical simulations, is the 3D scatter- 942

ing solution provided in Section 6, where the Advection Boundary Law is discretized and implemented on Electroacoustic Resonators, composed of a loudspeaker and four microphones. The 3D scattering results confirm that the enhanced isolation performances are still achieved despite the boundary discretization, and provide an intermediate step before the experimental validation of Section 7. An array of programmable Electroacoustic Resonators lining an acoustic waveguide allows to implement the Advection Boundary Law in real life. The measurements validate the Advection Boundary Law accomplishments in terms of enhanced isolation, passivity and non-reciprocal sound propagation, despite the physiological limitations of digital control algorithms.

Because of its non-natural and non-local character, special attention must be given when implementing the Advection Boundary Law. In this paper, we have provided a range of interpretational and numerical tools to guide the control users when implementing such special boundary control, in order to maximize its isolation performances, avoid non-passive behaviours, and/or achieve the desired non-reciprocal propagation. This first study has analysed the Advection Boundary Law in the plane-wave regime and in absence of mean flow. Such work has put the necessary bases for the Advection Boundary Law to tackle more complex guided propagation problems, including airflow convection and multi-modal propagation.

Appendix A Duct modes problem formulation

Consider an infinite duct of constant cross-section \mathcal{A} in the plane y, z (as in Fig. 1) with boundary $\partial\mathcal{A}$ and normal \vec{n} . Assuming a time-harmonic sound field in the usual complex notation ($+j\omega t$) in the duct, the wave equation reduces to the Helmholtz equation:

$$\nabla^2 \bar{p} + k_0^2 \bar{p} = 0. \quad (34)$$

Such sound field must also satisfy the generic BC $\mathcal{B}(\bar{p}) = 0$ on the wall $\partial\mathcal{A}$. The solution to this problem can be written as:

$$\bar{p}(t, \omega, x, y, z) = e^{j\omega t} \sum_{m=0}^{\infty} A_m \psi_m(\omega, y, z) e^{-jk_{x,m}(\omega)x}, \quad (35)$$

where $\psi_m(y, z)$, the so-called *duct modes*, are the eigenfunctions of the transverse Laplace operator reduced to \mathcal{A} satisfying the BC $\mathcal{B}[p] = 0$ on $\partial\mathcal{A}$, i.e. they are solution of the eigenvalue problem:

$$\begin{aligned} \nabla_{yz}^2 \psi_m(y, z) + (k_0^2 - k_{x,m}^2) \psi_m(y, z) &= 0 \quad \text{for } y, z \in \mathcal{A} \\ \mathcal{B}[\psi_m(y, z), k_{x,m}] &= 0 \quad \text{for } y, z \in \partial\mathcal{A}, \end{aligned} \quad (36)$$

where ∇_{yz}^2 denotes the Laplacian operator in y, z (following the notation of [33]), whose eigenvectors and eigenvalues are the duct mode shapes $\psi_m(y, z)$ and $(k_0^2 - k_{x,m}^2)$, respectively. Observe that for classical liners, the BC does not involve the axial wavenumber $k_{x,m}$.

We now formulate the duct mode problem in case of ABL as BC, in which the locally reacting liner is a special case (for $M_b = 0$). The duct-modes eigenvalue problem writes:

$$\nabla_{y,z}^2 \psi_m(y, z) - (k_0^2 - k_{x,m}^2) \psi_m(y, z) = 0 \quad \text{for } y \in \mathcal{A} \quad (37a)$$

$$\vec{n} \cdot \vec{\nabla} \psi_m(y, z) = -j\eta_{Loc} \left(k_0 - M_b k_{x,m} \right) \psi_m(y, z) \quad \text{for } y \in \partial\mathcal{A}. \quad (37b)$$

Notice the *non-standard* character of such eigenvalue problem, where the eigenvalue appears in the BC as well. Solutions for such eigenvalue problem can be found by FEs. The weak formulation of the eigenvalue problem of Eq.s (37) is reported in Eq.s (38), where $\hat{\psi}$ is the test function for the duct mode ψ_m . The integration by parts (application of Green formula) is given in Eq. (38b), and the final expression, with the assimilation of our BC, in Eq. (38c). Hence, our eigenvalue problem with an eigenvalue-dependent BC, can be solved directly in its weak-form, by FEs.

$$\int_{\mathcal{A}} \hat{\psi} \nabla_{y,z}^2 \psi_m \, dydz + (k_0^2 - k_{x,m}^2) \int_{\mathcal{A}} \hat{\psi} \psi_m \, dydz = 0 \quad (38a)$$

$$\int_{\partial\mathcal{A}} \hat{\psi} \partial_n \psi_m \, dydz - \int_{\mathcal{A}} \vec{\nabla}_{y,z} \hat{\psi} \cdot \vec{\nabla}_{y,z} \psi_m \, dydz + (k_0^2 - k_{x,m}^2) \int_{\mathcal{A}} \hat{\psi} \psi_m \, dydz = 0 \quad (38b)$$

$$-j\eta_{Loc} \left(k_0 - M_b k_{x,m} \right) \int_{\partial\mathcal{A}} \hat{\psi} \psi_m \, dydz - \int_{\mathcal{A}} \vec{\nabla}_{y,z} \hat{\psi} \cdot \vec{\nabla}_{y,z} \psi_m \, dydz + (k_0^2 - k_{x,m}^2) \int_{\mathcal{A}} \hat{\psi} \psi_m \, dydz = 0 \quad (38c)$$

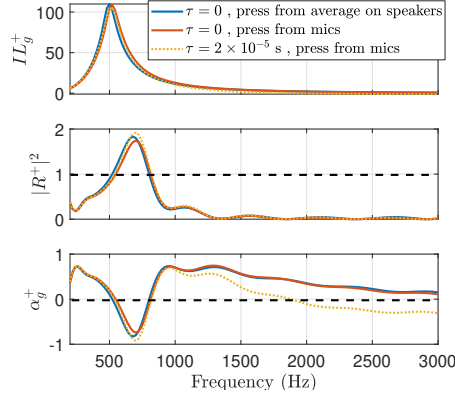


Figure 34. Scattering coefficients in a 3D waveguide of cross section width $h = 0.05$ m lined with ABL ($\mu_M = \mu_K = 0.5$, $R_d = \rho_0 c_0$, $M_b = -1$), in case of pressure average evaluation on speakers and no delay (in blue), in case of pressure evaluated from microphones averaging (see Fig. 25) and no delay (in red), and in case of pressure evaluated from corner microphones and with time delay (in yellow).

Appendix B Effect of discrete pressure evaluation and time delay in the 3D numerical model

In order to assess the effect of the pressure estimation from the 4 corner microphones on each ER, in case of ABL, in Fig. 34 we report the simulated scattering performances in a 3D waveguide, when \hat{p} and $\hat{\partial}_x p$ are retrieved from the average values on each ER disk (solid blue), or when \hat{p} and $\hat{\partial}_x p$ are obtained from the 4 corner microphones (solid red). In dotted yellow, we also report the simulations results when a time delay $\tau = 2 \times 10^{-5}$ seconds is considered in the controller. Observe that, employing the corner microphones to estimate \hat{p} and $\hat{\partial}_x p$ slightly affects the scattering performances around resonance and reduce the high-frequency passivity. The addition of a time delay in the control algorithm strongly affects the acoustical passivity at high frequencies, with α_g^+ and IL_g^+ becoming negative, as expected [16].

References

- [1] X. Ma, Z. Su, Development of acoustic liner in aero engine: a review, Science China Technological Sciences (2020) 1–14.

- [2] J. M. Hermiller, M. R. Maddux, Morphing Resonators for Adaptive Noise Reduction, *Acoustical Society of America Journal* 134 (2013) 3963.
- [3] S. J. Esteve, M. E. Johnson, Development of an adaptive Helmholtz resonator for broadband noise control, in: *ASME International Mechanical Engineering Congress and Exposition*, volume 47152, 2004, pp. 47–53.
- [4] A. Abbad, K. Rabenorosoa, M. Ouisse, N. Atalla, Adaptive Helmholtz resonator based on electroactive polymers: modeling, characterization, and control, *Smart Materials and Structures* 27 (2018) 105029.
- [5] H. F. Olson, E. G. May, Electronic Sound Absorber, *Journal of the Acoustical Society of America* 25 (1953) 1130–1136.
- [6] D. Guicking, E. Lorenz, An active sound absorber with porous plate, *Journal of Vibration and Acoustics, Transactions of the ASME* 106 (1984) 389–392.
- [7] M.-A. Galland, B. Mazeaud, N. Sellen, Hybrid passive/active absorbers for flow ducts, *Applied Acoustics* 66 (2005) 691–708.
- [8] B. Betgen, M. A. Galland, A new hybrid active/passive sound absorber with variable surface impedance, *Mechanical Systems and Signal Processing* 25 (2011) 1715–1726.
- [9] L. Cremer, Theory regarding the attenuation of sound transmitted by air in a rectangular duct with an absorbing wall, and the maximum attenuation constant produced during this process, *Acustica* 3 (1953) 249.
- [10] B. Tester, The optimization of modal sound attenuation in ducts, in the absence of mean flow, *Journal of Sound and Vibration* 27 (1973) 477–513.
- [11] A. J. Fleming, D. Niederberger, S. O. Moheimani, M. Morari, Control of resonant acoustic sound fields by electrical shunting of a loudspeaker, *IEEE Transactions on Control Systems Technology* 15 (2007) 689–703.
- [12] M. Furstoss, D. Thenail, M. Galland, Surface impedance control for sound absorption: direct and hybrid passive/active strategies, *Journal of Sound and Vibration* 203 (1997) 219–236.

- [13] D. J. Leo, D. K. Limpert, Self-sensing technique for active acoustic attenuation, in: Collection of Technical Papers - AIAA/ASME/ASCE/AHS/ASC Structures, Structural Dynamics and Materials Conference, volume 4, American Institute of Aeronautics and Astronautics, Reston, Virginia, 1999, pp. 2603–2610. URL: <http://arc.aiaa.org/doi/10.2514/6.1999-1530>. doi:10.2514/6.1999-1530.
- [14] E. Rivet, S. Karkar, H. Lissek, Broadband Low-Frequency Electroacoustic Absorbers Through Hybrid Sensor-/Shunt-Based Impedance Control, IEEE Transactions on Control Systems Technology 25 (2017) 63–72.
- [15] G. C. Goodwin, S. F. Graebe, M. E. Salgado, Control System Design, volume 27, Prentice Hall New Jersey, 2007.
- [16] E. De Bono, M. Collet, G. Matten, S. Karkar, H. Lissek, M. Ouisse, K. Billon, T. Laurence, M. Volery, Effect of time delay on the impedance control of a pressure-based, current-driven Electroacoustic Absorber, Journal of Sound and Vibration (2022) 117201.
- [17] E. T. J.-L. Rivet, Room Modal Equalisation with Electroacoustic Absorbers, Ph.D. thesis, EPFL, 2016. URL: <https://infoscience.epfl.ch/record/222866>. doi:10.5075/EPFL-THESIS-7166.
- [18] R. Boulandet, H. Lissek, S. Karkar, M. Collet, G. Matten, M. Ouisse, M. Versaevel, Duct modes damping through an adjustable electroacoustic liner under grazing incidence, Journal of Sound and Vibration 426 (2018) 19–33.
- [19] K. Billon, E. De Bono, M. Perez, E. Salze, G. Matten, M. Gillet, M. Ouisse, M. Volery, H. Lissek, J. Mardjono, Others, In flow acoustic characterisation of a 2D active liner with local and non local strategies., Applied Acoustics 191 (2022) 108655.
- [20] K. Billon, E. De Bono, M. Perez, E. Salze, G. Matten, M. Gillet, M. Ouisse, M. Volery, H. Lissek, J. Mardjono, Others, Experimental assessment of an active (acoustic) liner prototype in an acoustic flow duct facility, in: Health Monitoring of Structural and Biological Systems XV, volume 11593, International Society for Optics and Photonics, 2021, p. 115932L.
- [21] K. Billon, M. Collet, E. Salze, M. Gillet, M. Ouisse, M. Volery, H. Lissek, J. Mardjono, 2D active liner experimental results in acoustic flow duct facility, in: Smart Materials, Adaptive Structures and Intelligent

- Systems, volume 86274, American Society of Mechanical Engineers, 2022, p. V001T03A001. 1077
1078
- [22] K. Billon, M. Gillet, E. Salze, M. Volery, E. De Bono, M. Ouisse, H. Lissek, M. Collet, J. Mardjono, Smart acoustic lining for UHBR technologies engine: from the design of an electroacoustic metasurface to experimental characterization under flow, in: Active and Passive Smart Structures and Integrated Systems XVII, volume 12483, SPIE, 2023, pp. 390–396. 1079
1080
1081
1082
1083
1084
- [23] E. De Bono, M. Morell, M. Collet, E. Gourdon, A. Ture Savadkoohi, M. Ouisse, C. Lamarque, Model-inversion control to enforce tunable Duffing-like acoustical response on an Electroacoustic resonator at low excitation levels, Journal of Sound and Vibration 570 (2024) 118070. 1085
1086
1087
1088
- [24] C. E. da Silveira Zanin, A. Labetoulle, E. De Bono, E. Gourdon, M. Collet, A. Ture Savadkoohi, Experimental evidences of nonlinear programmable electroacoustic loudspeaker, Building Acoustics 30 (2023) 249–263. 1089
1090
1091
1092
- [25] M. Morell, M. Collet, E. Gourdon, A. T. Savadkoohi, Control of an acoustic mode by a digitally created Nonlinear Electroacoustic Absorber at low excitation levels: Analytical and Experimental results, in: Surveillance, Vibrations, Shock and Noise, 2023. 1093
1094
1095
1096
- [26] M. Morell, E. Gourdon, M. Collet, A. T. Savadkoohi, E. De Bono, NON-LINEAR DIGITALLY CREATED ELECTROACOUSTIC ABSORBER DESIGNED FOR ACOUSTIC ENERGY PUMPING (2023). 1097
1098
1099
- [27] M. Collet, P. David, M. Berthillier, Active acoustical impedance using distributed electrodynamical transducers, The Journal of the Acoustical Society of America 125 (2009) 882–894. 1100
1101
1102
- [28] S. Karkar, E. De Bono, M. Collet, G. Matten, M. Ouisse, E. Rivet, Broadband Nonreciprocal Acoustic Propagation Using Programmable Boundary Conditions: From Analytical Modeling to Experimental Implementation, Physical Review Applied 12 (2019) 054033. 1103
1104
1105
1106
- [29] E. De Bono, M. Ouisse, M. Collet, E. Salze, J. Mardjono, A nonlocal boundary control, from plane waves to spinning modes control., in: Active and Passive Smart Structures and Integrated Systems XVII, volume 12483, SPIE, 2023, p. 124831B. 1107
1108
1109
1110

- [30] E. de Bono, M. Collet, E. Salze, M. Ouisse, M. Gillet, H. Lissek, J. Mardjono, K. Billon, M. Volery, Advection boundary law for sound transmission attenuation of plane and spinning guided modes, in: *Forum Acusticum*, 2023. 1111–1114
- [31] R. Fleury, D. Sounas, M. R. Haberman, A. Alu, Nonreciprocal acoustics, *Acoustics Today* 11 (2015) 14–21. 1115–1116
- [32] A. N. Norris, Integral identities for reflection, transmission, and scattering coefficients, *The Journal of the Acoustical Society of America* 144 (2018) 2109–2115. 1117–1119
- [33] S. W. Rienstra, *Fundamentals of duct acoustics*, Von Karman Institute Lecture Notes (2015). 1120–1121
- [34] C. Bardos, G. Lebeau, J. Rauch, Sharp sufficient conditions for the observation, control, and stabilization of waves from the boundary, *SIAM journal on control and optimization* 30 (1992) 1024–1065. 1122–1124
- [35] P. M. Morse, Some aspects of the theory of room acoustics, *The Journal of the Acoustical Society of America* 11 (1939) 56–66. 1125–1126
- [36] B. Betgen, *Comportement d’un absorbant actif en écoulement: étude théorique et expérimentale*, Ph.D. thesis, 2010. 1127–1128
- [37] A. W. Guess, Calculation of perforated plate liner parameters from specified acoustic resistance and reactance, *Journal of Sound and Vibration* 40 (1975) 119–137. 1129–1131
- [38] U. Ingard, *Noise reduction analysis*, Jones & Bartlett Publishers, 2009. 1132
- [39] J. F. Allard, N. Atalla, *Propagation of Sound in Porous Media: Modelling Sound Absorbing Materials*, John Wiley & Sons, 2009. 1133–1134
- [40] A. A. Oberai, M. Malhotra, P. M. Pinsky, On the implementation of the Dirichlet-to-Neumann radiation condition for iterative solution of the Helmholtz equation, *Applied Numerical Mathematics* 27 (1998) 443–464. 1135–1138
- [41] U. Ingard, Influence of fluid motion past a plane boundary on sound reflection, absorption, and transmission, *The Journal of the Acoustical Society of America* 31 (1959) 1035–1036. 1139–1141
- [42] M. K. Myers, On the acoustic boundary condition in the presence of flow, *Journal of Sound and Vibration* 71 (1980) 429–434. 1142–1143

- [43] H. S. Ribner, Reflection, transmission, and amplification of sound by a moving medium, *The Journal of the Acoustical Society of America* 29 (1957) 435–441. 1144–1146
- [44] J. B. Keller, Reflection and transmission of sound by a moving medium, *The Journal of the Acoustical Society of America* 27 (1955) 1044–1047. 1147–1148
- [45] P. Filippi, A. Bergassoli, D. Habault, J. P. Lefebvre, *Acoustics: basic physics, theory, and methods*, Academic press, London NW1 7DX, UK, 1998. 1149–1151
- [46] G. Montseny, *Diffusive representation of pseudo-differential time-operators* (1998). 1152–1153
- [47] E. Rice, Modal propagation angles in ducts with soft walls and their connection with suppressor performance, in: *5th Aeroacoustics Conference*, 1979, p. 624. 1154–1156
- [48] R. Fleury, D. L. Sounas, A. Alù, Subwavelength ultrasonic circulator based on spatiotemporal modulation, *Physical Review B* 91 (2015) 174306. 1157–1159
- [49] M. L. Munjal, A. G. Doige, Theory of a two source-location method for direct experimental evaluation of the four-pole parameters of an aeroacoustic element, *Journal of Sound and Vibration* 141 (1990) 323–333. 1160–1163
- [50] L. L. Beranek, T. Mellow, *Acoustics: Sound Fields and Transducers*, Academic Press, Oxford OX5 1GB, UK, 2012. doi:10.1016/C2011-0-05897-0. 1164–1166
- [51] S. Devasia, Should model-based inverse inputs be used as feedforward under plant uncertainty?, *IEEE Transactions on Automatic Control* 47 (2002) 1865–1871. 1167–1169
- [52] E. De Bono, M. Collet, S. Karkar, G. Matten, H. Lissek, T. Laurence, Electroacoustic resonators: System identification and stability, in: *Proceedings of the 26th International Congress on Sound and Vibration, ICSV 2019, CONF*, Canadian Acoustical Association, 2018. 1170–1173
- [53] R. A. Pease, A Comprehensive Study of the Howland Current Pump A Comprehensive Study of the Howland Current Pump Applications for the Howland Current Pump AN-1515, *Most* 29 (2008) 12. 1174–1176

- [54] J. Steele, T. Green, Tame those versatile current source circuits, *Electronic Design* 61 (1992). 1177
1178